Cement & Concrete Research (2017) Accepted
https://doi.org/10.1016/j.cemconres.2017.09.012

Representative elementary volume (REV) of cementitious materials from three-dimensional pore structure analysis

M.H.N. Yio, H.S. Wong* and N.R. Buenfeld

Concrete Durability Group, Department of Civil and Environmental Engineering, Imperial College London, SW7 2AZ, UK

Abstract

The representative elementary volume (REV) is a fundamental property of a material, but no direct measurements exist for cementitious materials. In this paper, the REV of cement pastes with supplementary cementitious materials (GGBS, PFA, SF) was determined by analysing the three-dimensional pore structure (> 0.2 μm) using laser scanning confocal microscopy (LSCM). The effect of axial distortion inherent to LSCM on 3D pore structure was also investigated. A range of 3D pore parameters was measured using skeletonisation, maximal ball and random walker algorithms. Results show that axial distortion has insignificant effects on most parameters except Euler connectivity, average pore and throat volumes and directional diffusion tortuosities. Most pore parameters become independent of sampling volume at $\approx 60^3$ μm^3 except diffusion tortuosities and formation factor. The REV for porosity calculated based on a statistical approach at eight realisations and 5% relative error was found to be $\approx 100^3$ μm^3.

Keywords: *Microstructure (B); Image analysis (B); Transport properties (C); Cement paste (D); 3D pore structure*

1 Introduction

Representative elementary volume (REV), also known as representative volume element (RVE), is an important parameter for understanding and modelling the properties of multi-scale composite materials such as cement-based materials. The REV is the smallest volume over which a measurement or simulation can be carried out to produce a result that is representative of the macroscopic property. This is important because it is often difficult/impractical to experimentally capture or computationally generate composite materials at full length scales. Several definitions of REV exist, but there are two common requirements [1]: (1) the REV must be of the right size to contain sufficient microstructural features to depict the macroscopic property representatively, and (2) the REV is determined for a specified property and it is essentially independent of the sampling position within the material. Bear [2] presented the concept of REV graphically as shown in Figure 1. The fluctuations in the property of interest (e.g. porosity) reduce with increasing sampling volume and the volume at which fluctuations become insignificant is taken as the REV. For an inhomogeneous medium however, the property may gradually change again as the sampling volume increases further.

The REV depends on the length scale of the features of interest. Cement-based materials contain features ranging from nanoscale gel pores and hydrates to microscale capillary pores and millimetre-sized air voids and aggregate particles. Determining the REV at the concrete scale is relatively straightforward because one could simply carry out measurements on samples of varying sizes. However, it is much more challenging to do this at the scale of capillary pores. Yet, this is important because of its relevance to mass transport processes. The REV at the capillary pore scale is generally considered to be 100^3 μm^3. However, this value was derived from numerical modelling of computer generated 3D pore structures [3-5]. For example, Zhang *et al.* [4] adopted a numerical-statistical approach to determine the REV based on finite element simulated diffusion of tritiated water through 3D models of cement pastes (w/c 0.30 to 0.60) generated with HYMOSTRUC3D. Later, Ukrainczyk and Koenders [5] found that the REV of computer generated 3D pore structures is highly dependent on the employed numerical resolution, boundary conditions, initial particle size distribution of anhydrous cement particles and degree of hydration.

To the best of our knowledge, the REV for cementitious materials has never been measured experimentally at the capillary pore scale. This could be partly due to lack of suitable experimental techniques to characterise the 3D characteristics of pore structure at sufficiently high resolution. Recently, a new 3D imaging approach which combines laser scanning confocal microscopy (LSCM) with serial sectioning [6] has enabled 3D reconstruction of pore structure at submicron spatial resolution. The method involves stitching of sequential confocal stacks based on phase correlation

* Corresponding author. Tel: +44 (0)20 7594 5956.

E-mail: hong.wong@imperial.ac.uk

and so is able to image large volumes without resolution loss. Therefore, the method not only lends itself well for 3D pore characterisation, but also opens up possibilities for determining the REV of cement-based materials.

A number of issues need to be addressed to achieve this. For example, accurate segmentation of the pore structure from LSCM images is a prerequisite for successful analyses, but this is particularly challenging due to the complex boundaries between pores and solid hydration products. Uneven brightness that may occur along the depth of the reconstructed image further complicates the segmentation process. Fredrich [7] segmented the pore structure of Berea stone from 3D LSCM images using the local minima between solid and pore peaks in the image histogram as a threshold. Oh and Lindquist [8] have further developed a kriging-based method that determines the threshold based on minimum variance estimation within a pre-assigned threshold range, which also lies between the solid and pore peaks. However, the determination is not straightforward and is usually user-specified. Both methods are not applicable to this study because LSCM images of cement-based materials do not exhibit bimodal distribution in the histogram. Other approaches such as iterative k-means clustering also requires an a priori threshold to be estimated [9].

Furthermore, the process for quantitative analysis of the 3D pore structure based on images reconstructed by such a method has not been established to date. It is also well recognised that 3D LSCM images suffer from distortion in the optical (axial) axis because of two main reasons [10, 11]. First, the resolution is inherently anisotropic along the optical axis due to the elongation of point spread function (PSF). Second, mismatch of refractive indices between the immersion medium and the sample or within the sample itself can lead to severe spherical aberrations. Such distortions can produce misleading results when volumetric measurements are made. In biological imaging, the axial distortion caused by refractive index mismatch can be corrected empirically by inserting fluorescent microspheres of known geometries into the specimen to measure the elongation [12, 13]. However, this approach is unsuitable for hardened cement-based materials. While it may be possible to place 'micro-standards' in the fresh mix, they will either end up in the pore space or be engulfed by hydration products and therefore cannot be distinguished in hardened cement paste. Depending on the size of the standards, the resulting microstructure may also be altered owing to the formation of new interfaces. Moreover, these standards are required in large quantities and dispersed within the system to ensure a homogeneous correction.

The main aim of this paper is to: (1) study the effects of axial distortion in LSCM images on 3D pore parameters, and (2) estimate the REV for different pore parameters and cementitious systems. A method for pore segmentation and protocol for charactering the 3D pore structure was first developed. Then, the methods were validated on measurements of ideal 3D model structures. Finally, the methods were applied to quantify over twenty 3D pore structure of real cementitious samples in order to study the effects of axial distortion and to determine the REV. A range of blended cement pastes containing CEM I, silica fume, pulverised fuel ash and ground granulated blastfurnace slag cured to 7 and 90 days were tested.

2 Experimental

2.1 Materials and sample preparation

Four cement pastes containing CEM I and CEM I blended with silica fume (SF), pulverised fuel ash (PFA) or ground granulated blastfurnace slag (GGBS) were prepared and cured for 7 and 90 days to produce samples with a range of microstructure. Mix proportions are shown in Table 1. The oxide compositions and properties of the cementitious materials are given in Table 2. The Bogue composition of CEM I was 53.1% C_3S, 19.1% C_2S, 10.8% C_3A and 7.2% C_4AF. The fineness and specific gravity of the CEM I were 291 m^2/kg and 3.06 respectively.

All wet-mixing was done in a Hobart mixer for 4 min. PFA and GGBS were dry-mixed with CEM I for 1 min before water was added. For the mix with SF, a polycarboxylate-based superplasticiser was added to the water at 0.4 wt. % binder and pre-mixed with SF for 1 min to disperse agglomerated particles. All mixes were cast in steel moulds of 100 mm diameter × 25 mm height and compacted in two layers using a vibrating table. Immediately after casting, the samples were covered with plastic sheets and wet hessian to prevent loss of moisture, and left to harden at 20ºC. After 24 hours, the samples were demoulded and cured in a fog room at 100% RH and 20ºC for 7 and 90 days.

For each mix and curing age, four replicate discs were prepared; one for LSCM imaging and three for mass transport measurements, the latter will be reported in a separate publication. A slight amount of bleeding was observed after casting therefore two additional disc samples were prepared per mix to measure bleed water. The bleed water on the sample surface was collected by pipette and measured periodically in accordance with BS EN 480-4:2005 [14]. The corrected free w/b ratios for each mix are given in Table 1.

2.2 Samples for microscopy

After curing, a block (40×20×8 mm^3) was extracted from the centre of each disc (Figure 2) using a diamond saw (Logitech GTS1) for imaging. The blocks were then placed in sealed environmental chambers containing saturated

potassium dichromate ($K_2Cr_2O_7$) for conditioning at 55% RH, 20ºC. The chambers were equipped with motorised fans to generate circulating air and soda lime to minimise carbonation. The blocks were conditioned until mass loss was no more than 0.01%/day. This typically took around 90 days.

Following conditioning, the blocks were fully impregnated with fluorescein-doped epoxy following the method described in Wong and Buenfeld [15]. The epoxy (Struers EpoFix, refractive index 1.578) was doped with fluorescein (C.I. Solvent Yellow 43) at 0.05 wt. %, then mixed with hardener at 25:3 mass ratio and thinned with toluene at 5% wt. Earlier work [6] found that a 0.05 wt. % dye concentration produced maximum fluorescence intensity under the imaging conditions described in Section 2.3.

The blocks were placed under vacuum (-1 bar) for an hour to remove air and then submerged in fluorescein-doped epoxy without breaking the vacuum. Vacuum was then released to force the epoxy into the blocks. Immediately after that, the blocks were pressurised with compressed air at 2.5 bars for 2 hours to complete the impregnation. Finally, the blocks were ground and polished using successively finer abrasive grit sizes of 30, 18, 14, 9, 6, 3, 1 and 0.25 µm until a flat and highly reflective surface was achieved.

2.3 LSCM and 3D pore reconstruction

3D images of the pore structure were reconstructed using the method described in Yio *et al.* [6]. This combines fluorescence LSCM with serial sectioning to produce a series of overlapping 3D confocal Z-stacks, which are then aligned and stitched based on phase correlation. A Leica TCS SP5 microscope equipped with HCX PL APO 40× (NA 1.25) oil immersion objective was used for imaging. The pinhole aperture size was set at 0.3 Airy unit. A 488 nm argon laser at 15% intensity was applied to induce fluorescence. At these settings, the theoretical spatial XY and Z resolutions were 0.156 and 0.534 µm respectively. These were calculated according to the Rayleigh criterion (Pawley, 1995) from the numerical aperture (NA) of the objective lens, refractive index of immersion oil (1.518), laser excitation wavelength and pinhole aperture (see [6] for details).

The emission band was set to range from 500 to 600 nm to ensure that all emitted fluorescence was captured. A zoom factor of 1.8× was applied to give a field of view of 215 × 215 µm^2 and images were digitised to 2048 × 2048 pixels. The final voxel size was 0.105 × 0.105 × 0.1 µm^3. Based on the Nyquist theorem, the smallest pore that can be resolved in the XY and Z direction is ≈ 0.242 µm (2.3× voxel width) and ≈ 0.534 µm (2.3× voxel depth) respectively. A 2× line averaging, 400 Hz scan speed and a 3D median-filter with 1 × 1 × 2 voxel radii were applied to ensure good signal-to-noise ratio.

Two spots ≈ 5 mm apart (namely A and B) near the centre of each block were imaged (Figure 2). Serial sectioning was done by grinding with 15 µm diamond on a Struers LaboPol-5 machine at low applied force (7N) and rotation (50 rpm). Depending on the sample mix and age, grinding time was varied between 1 to 4 s per direction to remove an average of 1.83 to 3.57 µm thick material per step. The sample was imaged after each grinding step to capture a 3D Z-stack of ≈ 10 µm thick. Well-focused images with high signal-to-noise ratio from each stack were selected, aligned using image registration with StackReg [16] and stitched using Pairwise stitching [17]. The process of sectioning, imaging, alignment and stitching was repeated until the total thickness of the reconstructed image ranged from 108 to 150 µm (see Table 3). This required stitching of 40 to 62 stacks. The average overlapping regions between stacks ranged from 34.3 to 47.9% and the average correlation coefficients (R) ranged from 0.87 to 0.93, indicating good accuracy of the reconstruction process for all samples. The final area of the reconstructed image (≈ 190 × 190 µm^2) was smaller than the field of view (215 × 215 µm^2) due to the loss of a small region around the edges during alignment (Table 3). Full details of the image acquisition process are given in Yio *et al.* [6].

2.4 Pore segmentation

A typical LSCM image of hardened cement paste (P0.45 7d) and its brightness histogram are shown in Figure 3. The same area imaged with backscattered electron (BSE) microscopy is also shown. Similar features can be seen in both images, giving confidence in the LSCM technique. However, slight differences are inevitable due to the fact that the images were not captured at the exact same plane. The LSCM image was obtained slightly beneath the sample surface for even and optimum brightness, while the BSE image is of the sample surface.

Note that bright green pixels in the LSCM image are pores while dark pixels are solids. Unreacted cement grains (AH) are dense, thick and non-porous, so they do not fluoresce and appear black. However, hydration products such as calcium silicate hydrates (C-S-H) are less dense and have an amorphous nano-porous structure. The C-S-H may appear brighter due to a slight detectable subsurface fluorescence occurring within the optical section (Z-stack). Pores approaching the resolution limit or smaller than the voxel size will also show intermediate brightness levels due to diffraction and mixing of signals from several phases. As such, the brightness histogram of LSCM shows a peak

representing solids, with a broad shoulder at the higher end of the grey scale with no distinct peak for pores due to overlapping grey levels between some phases.

All these create uncertainties when selecting the threshold to segment pores from solids. Realistically, a perfect segmentation is not possible, but an objective and repeatable approach applied to all samples is needed. Due to the lack of a local minimum in the histogram, simple thresholding based on peaks and valleys, or the overflow method [18, 19] do not work well. Various approaches commonly applied to fluorescent images were tested (e.g. Otsu's method [20], IsoData [21], maximum entropy [22] and triangle method [23]). It was found that the moment-preserving method by Tsai [24] was able to yield the most satisfactory results, based on visual comparison between the original and segmented LSCM and backscattered electron images. The method is deterministic and does not require iterations. It computes the threshold by retaining the first three moments of the original image in the binarised image. The first moment is the mean grey value whereas the second and the third moments describe the variance and skewness of the image histogram respectively [25]. It is also worth noting that this method has been applied successfully to 3D fluorescence LSCM images of a silica monolith's skeleton [26] with pores of similar sizes to cement paste. A brief description of the method is given in Appendix I.

Prior to segmentation, contrast limited adaptive histogram equalisation (CLAHE) [27] was applied to each image slice to enhance the contrast of very fine pores. A block of 23 pixels (10× the resolvable pore size) was used to define the local region for histogram equalisation. The number of histogram bins used was 256 and the maximum slope to restrict maximum contrast change was set to 1.5. All operations were slice-wise and performed using Fiji (v.1.51d) [28]. Following pore segmentation, 3D morphological dilation and erosion with a kernel diameter of 3 voxels was applied to the entire image to fill in small holes, remove noise and smooth edges of the pore structure. Given that the segmentation process was slice-wise, a second 3D median filter with radii of 1 × 1 × 2 was applied to eliminate discontinuities along edges of the segmented pores in the axial direction.

2.5 Quantitative 3D pore structure analysis

Over twenty 3D pore parameters, summarised in Table 4, were measured. These include: a) global parameters such as porosity, specific surface area and pore size distribution; and b) topological parameters that describe connectivity and degree of convolution (e.g. tortuosity). Three methods were used. The first was BoneJ [29] that consists of a set of commands including medial-axis skeletonisation [30] which finds the skeleton running through the entire pore structure. The second method was the modified maximal ball algorithm [31] which extracts the pore network by fitting spheres of variable sizes into the pore space and ranking them accordingly to determine the largest spheres which form the largest pores connected by smaller spheres which form the pore throats. The third method consisted of two Mathematica® programmes [32] which run cluster labelling to detect connected pore voxels and random walk simulations. Details of these can be found in their respective references.

The skeleton tortuosity determined using the medial axis-thinning algorithm is a direct measure of the crookedness of the pore structure. It is calculated as [33]:

$$\tau_s = \frac{\sum_{i-1}^{j} L_e}{\sum_{i-1}^{j} L_a} \qquad \text{Eq. (1)}$$

Where i is the index of skeleton branch, j is the total number of skeleton branches, L_e and L_a are the actual and Euclidean lengths of each skeleton branch respectively. Another measure of the pore geometrical complexity is the diffusion tortuosity, which is based on the ease of self-diffusion of random walkers defined as follows:

$$\tau_D = \frac{D_f}{D(t)} = \frac{a_1^2}{\frac{d\left(r(\tau_t)^2\right)}{d\tau_t}} \quad \text{as } t \text{ and } \tau_t \to \infty \qquad \text{Eq. (2)}$$

Where D_f and $D(t)$ are the self-diffusivity (m^2/s) of random walkers in free space and pore space as a function of time (t) respectively, a_1 is the dimension of a cubic voxel (m) and $r(\tau_t)^2$ is the mean square displacement of the walkers as a function of a unit time (τ_t). By assigning a value of 1 to a_1, the mean square displacement becomes dimensionless and so is the diffusion tortuosity. Unless otherwise stated, a total of 20,000 random walkers and 1×10^7 time steps (τ_t) were used in the simulations so that the walkers experienced the full tortuosity of the pore structure. The time derivatives of the mean square displacements were calculated from the fitted slope of the mean square displacement vs. lattice walk time curve. The slopes were fitted for $\tau_t > 2\times10^6$ and $\tau_t > 4\times10^6$ for 7 and 90-day samples respectively. This was to avoid

unrestricted diffusion of the walkers during the early stages of simulation where most walkers rarely collided with the pore walls. By breaking down the scalar mean square displacements into the X, Y and Z axes, directional diffusion tortuosities can also be calculated.

Another relevant parameter is the formation factor (*F*), which is calculated based on the Nernst-Einstein relationship as [34-36]:

$$F = \frac{\sigma_o}{\sigma} = \frac{D_o}{D} = \frac{\Phi_p}{\tau_D^2} \qquad \text{Eq. (3)}$$

Where σ_0 and σ are the electrical conductivities (S/m) of pore solution and saturated material respectively, D_0 and D are the free and intrinsic diffusivities (m^2/s) of the bulk system respectively, Φ_p is the accessible porosity and τ_D is the scalar diffusion tortuosity. There is no general consensus as to whether or not the diffusion tortuosity should be squared. Indeed, several versions of the above relationship exist where tortuosity is unsquared or square rooted, as summarised by [37]. However, it was observed that Eq. 3 gave better predictions of transport properties (to be published).

Two workstations were used to run the algorithms: one is equipped with an Intel® Xeon™ CPU E5-1650 0 at 3.2 GHz processor with 32 GB RAM running on 64-bit Windows 7 Enterprise and the other is equipped with an Intel® Core™ i7-4770 CPU at 3.4 GHz processor with 16 GB RAM running on 64-bit Windows 8 Home.

2.6 Axial distortion

A systematic analysis was performed to investigate the effect of axial elongation in 3D LSCM images on the measured pore parameters (Table 4). A sub-volume with an area of 100 μm^2 was cropped from the main 3D images of P0.45 7d. The voxel depth was first factored by 1.05 to correct for the mismatch of refractive indices between the immersion oil and epoxy in the pore structure [6]. Following that, the sub-volume was segmented using the method described in Section 2.4. A compression factor of 0.25, 0.50, 0.75 and 1.00 was then applied to the voxel depth to create a series of compressed image volumes with total thicknesses of 35, 70, 105 and 140 µm respectively. These image volumes were further re-sliced prior to 3D median filtering to yield isotropic voxels of 0.105 μm^3 for analysis with the methods presented in Section 2.5. All other samples were analysed for the extreme compression factor of 0.25 and 1.00.

Having completed the above, a suitable correction factor for elongation across all samples was determined using spherical PFA particles in P0.45 PFA 7d and 90d as benchmarks. The principle is analogous to that of microspheres but in this case, the exact sizes of PFA particles are unknown. PFA particles are intrinsically perfect spheres and hence their aspect ratios in the XY and Z directions are approximately equal to 1. This enabled a correction factor to be determined by measuring the aspect ratios of many PFA particles as a function of reducing voxel depth without knowing their exact sizes.

In total, 80 PFA particles were randomly selected per sample (40 for each curing age) for measurements. The voxel depth was gradually compressed at intervals of 0.05. At each compression factor, the aspect ratios of all 80 particles were measured in the orthogonal views (XZ and YZ planes). Due to complexity of the microstructure, it was difficult to use a tracing tool to delineate particle boundaries for measurement. Instead, the 'Oval selections' tool in Fiji was used to fit ellipses to the PFA particles and the aspect ratios were recorded. The compression factor that gave the average aspect ratio closest to 1 was adopted as the correction factor.

2.7 Determination of representative elementary volume (REV)

The REV for different cementitious systems were determined using a statistical approach. Four sub-volumes of 100^3 μm^3 were cropped from the imaged spots and segmented. Following that, smaller sampling volumes of 20^3, 40^3, 60^3 and 80^3 μm^3 were extracted from their centres (Figure 4). Thus, a total of 20 sampling volumes (10 each for spots A and B) were analysed per sample. The 100^3 μm^3 sampling volumes were selected diagonally to each other and so they overlap slightly (no more than ≈7%). In some cases, the total thickness of the image volume was less than 100 µm after being corrected for axial distortion (see Table 3 & Section 3.4). The voxel depth was also resliced to give isotropic voxels (0.105^3 μm^3). A total of 160 sub-volumes were analysed for the entire study.

The statistical approach enables the REV to be defined for a given property, number of realisations (or number of image volumes analysed, *n*) and a chosen accuracy of the estimate (indicated by relative error, ε). For example, the REV (m^3) based on porosity can be calculated using Eq. (4) and Eq. (5) [38, 39]:

$$V_{REV} = \frac{4(1 - \Phi_T)A_3}{n\Phi_T \varepsilon^2} \qquad \text{Eq. (4)}$$

Where Φ_T is the 'true' total porosity (taken as the mean porosity of the main image volume from spots A and B ≈ 190 × 190 × 100 µm^3) and A_3 is related to the variance of the porosities ($D_p^2(V_I)$) measured from n realisations for each volume size (V_I, m^3), and was determined by fitting Eq. (5) to measured data:

$$D_p^2(V_I) = \frac{\Phi_T(1-\Phi_T)A_3}{V_I} \qquad \text{Eq. (5)}$$

3 Results

3.1 Pore segmentation

Figure 5 shows example images (XY plane) of a relatively porous (P0.45 PFA 7d) and relatively dense (P0.45 SF 90d) system segmented using the proposed method described in Section 2.4. Generally, both systems are well-segmented. Features with defined boundaries such as the PFA and anhydrous cement (AH) particles are visible. Pores as small as ≈ 0.2 µm are also segmented as shown by arrows in Figure 5c and d. This demonstrates the ability of the applied methodology (Section 2.4) to segment very fine features. Several hollow shell pores or 'Hadley' grains are also visible [40]. However, low contrast features such as the shells of some 'Hadley' grains (marked by red boxes in Figure 5a and b) and some pores nestled in solids (marked by red boxes in Figure 5c and d) may not be adequately segmented.

Figure 6 shows the pore structure of P0.45 PFA 7d and P0.45 SF 90d in three-dimensional views. A small volume of interest (30^3 µm^3) was cropped from Figure 5 as an example to highlight the pore topology. Note that although the segmentation was performed slice-wise in the XY plane, pore edges in the Z plane appear smooth with no apparent discontinuities. A compression factor of 0.725 was applied to these images (see Sections 3.2 and 3.3). The largest connected pore and its corresponding skeleton determined by mapped-labelling and medial axis thinning algorithms show that P0.45 PFA 7d is more percolated than P0.45 SF 90d. The pore networks extracted by the maximal ball algorithm also indicate that the pores and throats of P0.45 PFA 7d are much larger than those of P0.45 SF 90d, consistent with our expectation.

3.2 Validation on ideal 3D pore structures

The algorithms described in Section 2.5 and Table 4 were tested on nine 3D pore models constructed from spheres and cylinders of known sizes to represent pores and throats respectively. This is essentially to check that the algorithms are correct before applying them to actual 3D pore images for determining REV. The ideal pore models were generated using 3D Draw Shape and Line [41] in Fiji. 3D dilation and erosion were applied as in Section 2.4. Three pore configurations were considered: (i) pores attached, (ii) pores linked by short throats and (iii) pores linked by long throats. Details of the nine pore models are given in Table 5 and Figure 7. The measured total volume, surface area, pore and throat sizes, throat length, skeleton length and distance between pore to pore centres were compared with theoretical values in Figure 8. Note that the theoretical values were calculated by assuming that the sphere and throat surfaces were smooth and continuous. Overall, there is a good agreement between measured and calculated values.

All three methods (BoneJ, cluster labelling and maximal ball) gave the same total pore volumes, but slightly higher than theoretical values by 5.07% on average. This is due to the fact that the pore models are voxelised rather than having continuous smooth surfaces assumed in calculations. The measured total surface areas were on average higher than calculated values by 1.62% with BoneJ (marching cube algorithm) and 50.8% with cluster labelling. This is because triangular isosurface meshes used in BoneJ gave a better representation of curved surfaces compared to discretised voxels assumed in cluster labelling. The average pore sizes were slightly underestimated (-2.07%) by the maximal ball algorithm because the upper-limit radius of maximal ball is defined as the Euclidean distance from the centre voxel to the nearest grain voxel [31]. However, the average throat radius and throat lengths were overestimated slightly (8.28% and 15.9% respectively) because the throats in "pores attached" models (a, b, c) were enlarged during erosion/dilation due to close proximity between spheres (2 voxels). The total pore centre-to-centre lengths were accurately measured by maximal ball (1.52% mean error) while the total skeleton length obtained by medial axis thinning (BoneJ) had a slightly larger mean error of 5.21%. This was because the skeletonised branches were not straight within the spheres. Nevertheless, the topologies of all pore structures were well-preserved in the skeleton image as seen in Figure 7.

3.3 Effect of axial distortion

Figure 9 shows the XZ plane of a sampling volume of P0.45 7d subjected to different axial compression factors. In can be seen that the pores appear stretched in the vertical direction when no axial compression was applied (1.00) and appear compressed when the applied factor was 0.25. Visually, an axial compression between 0.50 to 0.75 give the least distorted image. A more detailed quantitative assessment of this will be given in Section 3.4.

Figure 10 shows the effect of axial compression on measured pore parameters (Table 4). Note that the results are normalised to that of no compression. It can be seen that many pore parameters are insensitive to axial compression. These include total porosity, accessible (largest connected) porosity, percolation connectivity and skeleton tortuosity. Other parameters such as specific surface, shape factor, coordination number, pore and throat radii showed only a slight fluctuation. These parameters remain relatively constant because the pore and total sample volumes changed at equal proportion with axial compression. Similarly, the lengths and Euclidean distances of pore skeleton branches reduced at the same magnitude with increasing compression.

As expected, the average pore size, skeleton branch length, volumes and lengths of pores and throats decreased with increasing compression. This is because of the reduced dimension (shortened pore length) in the Z direction. Euler connectivity increased with compression because the contribution of the pore structure to the Euler characteristic of the entire image increased (see Table 4 and Odgaard and Gundersen, 1993 for details). The directional diffusion tortuosities were also significantly affected by compression (Figure 10c). This is because directional diffusion tortuosities were calculated as (1/3) / fitted slope of random walks in the X, Y and Z directions. Compression causes the cumulative mean square displacement of walkers (after a given simulation time) to reduce in the Z direction and increase in the XY direction. This led to increased Z tortuosity and reduced XY tortuosity.

Figure 10d presents the fitted slopes to mean square displacement vs. lattice walk time curves for calculating directional diffusion tortuosities. The larger the fitted slope, the lower the diffusion tortuosity. It is clear from the figure that with no compression, the contribution from the Z direction outweighs those from the XY directions, indicating an elongation of the pore structure in the original image. Axial compression decreases the contribution from Z direction and increases those from XY. Given that scalar diffusion tortuosity is equal to the sum contributions from all three directions, it remained relatively stable with increasing compression (Figure 10c). Similarly, the formation factor is insensitive to compression because it is calculated from scalar diffusion tortuosity and accessible porosity (Eq. 3).

The effect of axial distortion on all other samples was investigated for compression factors of 0.25 and 1.00. The porosities of these samples ranged from 14.2% to 26.4%. The results, summarised in Appendix II, are consistent with the findings from P0.45 7d above that many pore parameters are relatively insensitive to axial distortion. The parameters most affected are Euler connectivity, pore and throat volumes, and directional tortuosities.

3.4 Proposed correction factor for axial distortion

Figure 11 shows the XY and XZ planes of a PFA particle from P0.45 PFA 90d subjected to axial compression. The uncompressed XY plane clearly shows that the particle is a perfect sphere of diameter ≈ 3.7 μm. However, in the XZ plane, the particle appears prolate and changes progressively to spherical then oblate when the axial compression factor increased to 0.5. The optimum compression factor that restored the particle to a sphere was approximately 0.7 (marked by a red box).

Figure 12a shows the average aspect ratios of 80 PFA particles from P0.45 PFA at 7 and 90 days measured as a function of increasing axial compression. The error bars represent the 95% confidence interval of the average based on Student's *t* distribution. The particle diameters determined from the minor axis of fitted ellipse without axial compression ranged from 9 to 276 μm, thus a wide range of feature size was sampled. Note that this range of particle sizes are relatively large in comparison to the Z-resolution or the PSF. Thus, very fine features close to the Z resolution or PSF would remain elongated. The results show that the smallest aspect ratio was achieved with axial compression ≈ 0.75 to 0.80 at 7 days, and ≈ 0.65 to 0.70 at 90 days. This suggests that the axial distortion was slightly more severe at 90 days. Taking all data into consideration, the optimum compression was between 0.70 and 0.75 (Figure 12a).

Another approach to estimate the optimum correction factor was to measure the amount of compression required to give the smallest aspect ratio for every PFA particle. The results are presented as a frequency distribution histogram in Figure 12b. A spread of values is observed for both ages, indicating heterogeneity of the axial distortion. Nevertheless, the histograms show a peak at compression factors of 0.70 and 0.75, where most particles (55% for 7-day and 60% for 90-day) were restored to spheres. Given that the optimum compression factors are so close, it is proposed that an average value of 0.725 is adopted as the correction factor for all samples.

3.5 Representative elementary volume

The effect of increasing sampling volume on the measured pore parameters (Table 4) is shown in Figures 13 to 15. The total time steps (τ_t) used for random walk simulations were 2, 4, 6, 8 and 10×10^6 for sampling volumes of 20^3, 40^3, 60^3, 80^3 and 100^3 μm^3 respectively while the total number of random walkers was kept at 20,000. Each data point is an average of four measurements (two from each imaging spot A & B) and normalised to that of the 100^3 μm^3, acting as a benchmark. The error bars mark the maximum and minimum values. Note that the scale used on the Y-axes varies between plots and the X-axis represents the linear dimension of the image cube (= volume$^{1/3}$).

The results show large scatter for all pore parameters when measurements were made on small image volumes (20^3 to 40^3 μm^3). There is also huge variability in the measured values and in some cases, the largest percolated pore structure was found to span the image volume in one or two directions only, instead of all three (X, Y and Z) directions. However, the degree of scatter for all pore parameters reduced significantly with increasing sampling volume. Most parameters became relatively constant (within ± 10% of the benchmark values) at 60^3 μm^3 except for the scalar diffusion tortuosity and formation factor (Figure 15).

The REV for porosity was calculated for all systems using Eq. (4) for a range of relative errors (ε = 1.0, 2.5, 5.0, 7.5 and 10.0%). The 'true' porosity Φ_T was taken as the mean total porosity of the main image volume (≈ 190×190×100 μm^3) of spots A and B. The integral range A_3 was determined from Eq. (5) by curve fitting the variance of measured porosities to image volume as shown in Figure 16a. The best fit R^2 values for all curves were > 0.93, except for P0.45 GGBS 90d whose variances were relatively small and showed poor linearity with image volume. Overall, A_3 increased with increase in porosity variance. As such, A_3 is an indicator of pore structure heterogeneity. This can also be seen in Figure 16b showing a positive correlation between A_3 and length of REV for all systems (n = 8 and ε = 5.0%).

The calculated REVs are presented in Figure 17. As expected, the size of the REV decreases with increasing number of realisations and relative error. This is because the measured pore parameters become more statistically representative if a greater number of images is analysed and if the tolerable error in the measurement is higher. There is no discernible effect of curing age on the REV. For a single realisation (n = 1) and relative error of 1%, the REVs ranged from 354^3 μm^3 (P0.45 GGBS 7d) to 626^3 μm^3 (P0.45 SF 90d), excluding P0.45 GGBS 90d whose A_3 value was uncertain. However, as n increased to 8 and ε increased to 5%, nearly all REVs fell below 100^3 μm^3 except for P0.45 PFA 90d (101^3 μm^3), P0.45 SF 7d (107^3 μm^3) and P0.45 SF 90d (107^3 μm^3). To achieve a REV of 100^3 μm^3 and maintaining the relative error at 1%, the number of realisations required ranged from 44 (P0.45 GGBS 7d) to 248 (P0.45 SF 90d), excluding P0.45 GGBS 90d. However, the requirement for such a high number of image volumes is not currently practical for 3D imaging.

4 Discussion

The proposed pore segmentation method may produce slight under- or over-segmentation with very low contrast features. The CLAHE operation enhances the local contrast of these features, but noise may also be enhanced and this is an inevitable side effect. The segmentation process may be affected by artefacts such as scratches and fall-out particles which occur during the sectioning process. Nevertheless, such artefacts are localised on the polished surface and will not affect overall results. This is because surface artefacts are removed once the Z-stacks are overlapped to reconstruct the 3D image. Finally, it should be recognised that a perfect segmentation method does not exist, but the approach proposed in this paper provides an objective means to pore segmentation.

Given that only pores connected to the sample surface and interconnected within the sample can be filled with fluorescein epoxy, the largest remaining pore following mapped-labelling or cluster labelling processes is effectively interconnected. Hence, no further segmentation such as watershed is needed to split the pore into sub-clusters. Clearly, pores which are smaller than the spatial resolutions of LSCM (≈ 0.2 μm in XY and ≈ 0.5 μm in Z direction) may not be resolved properly. However, these pore sizes are already much finer than those resolvable by conventional X-ray μCT.

It has recently been shown by [42] that the critical pore entry diameter measured with mercury intrusion porosimetry (MIP) for 28-day white cement pastes cured underwater occurred at a few tens of nanometres. Such pores are obviously much smaller than the pores considered in this study. However, the very different appearance of pore structure obtained from MIP and other imaging techniques such as LSCM may not be as inconsistent as it seems. As evident from LSCM (Figure 3), large pores may in fact be interconnected through much smaller pores within the C-S-H, termed as 'interhydrate' pores [43]. These are probably within regions of hydrates that exhibit intermediate brightness levels in the LSCM images. However, it should be emphasised that direct comparison between MIP and LSCM is not straightforward, as these techniques are different in terms of working principle, sample preparation (pre-drying techniques) and data interpretation.

Different cementitious systems tend to exhibit slightly different levels of axial distortion in LSCM images. Therefore, the proposed axial correction factor of 0.725 is an approximation. Ideally, a specific correction factor for each system should be determined. As mentioned in the Introduction, it is impractical to use micro-standards for this purpose. An alternative approach is to use random walker to find the optimal compression factor that gives equal directional diffusion tortuosities by trial-and-error. However, such a method is retrospective and is valid only if the pore structure is perfectly isotropic. Moreover, the axial distortion within a system is spatially variable depending on local porosity, phase density and refractive index. Nevertheless, as shown in Section 3.3, the major pore parameters such as porosity, specific surface, average pore and throat sizes, percolation connectivity and scalar diffusion tortuosity are not significantly affected by axial distortion, and therefore knowing the exact correction factor is not critical. The measured REV is not influenced by the choice of correction factor.

The determination of REV relied on averaging of four replicates and the results show this is adequate (small error bars). The obtained REVs based on the change in measured pore properties with increasing image volume for CEM I systems were between 60^3 to 100^3 µm^3. These are generally in line with those determined from computer-generated 3D pore structure of pastes, e.g. Garboczi and Bentz [3] and Zhang *et al.* [4], with pre-defined water/cement ratio and cement particle size distribution and composition. Determination of REV from such models is also based on a statistical approach, where the fluctuations in the property of interest are quantified for a number of sampling volumes with increasing volume size until the property reaches a desired accuracy. Nevertheless, the sampling volumes are individually generated in modelling whereas those from experiments (e.g. Rolland du Roscoat *et al.* [39] and Mendoza *et al.* [44]) are usually sampled within the main domain at increasing length due to impracticalities with obtaining large number of datasets, as was the case in this study.

One may argue that the observed convergence in the measured property (Figs. 13, 14 &15) was down to the increasingly large occupation of the sampling volumes within the entire domain. It should, however, be noted that the occupation of the sampling volumes (20^3, 40^3, 60^3 and 80^3 µm^3) within the 100^3 µm^3 image volume was only 51.2% at most. To further support our findings, the average porosity measured from each sampling volume is normalised to the porosity measured from the main image volume (≈ 190×190×100 µm^3). Figure 18 plots the normalised porosity against the size ratio of sampling volume to main image volume. Results show that the porosities become relatively constant and fall within ±0.1 when the sampling volume is at only ≈ 6 to 30% of the main image volume. This corresponds to a sampling volume of 60^3 to 100^3 µm^3, which confirms the findings from Section 3.5.

Given that a range of binder type, curing age and pore structure was covered in this study, the findings obtained should be relevant to other systems. However, it is important to note that these results were obtained from cement pastes, based on measurements made at two locations separated by a 5 mm distance. The REVs determined are likely a lower limit (see Figure 1) [2] since larger scale spatial variation may exist, but not be accounted for. Concretes and mortars are inherently even more heterogeneous than cement pastes because of the presence of aggregate particles, interfacial transition zone (ITZ) and defects such as microcracking and segregation. Therefore, pore structure variation occurs over larger length scales and the REV of these materials will be greater than for cement pastes. However, as explained in the Introduction, determining the REV at concrete scale is less complicated because one can simply conduct tests on samples of varying sizes. For example, 3D numerical modelling of mortars and concretes containing different aggregate particle shapes with ITZ show that a numerical sample size of at least 2.5× the largest aggregate particle is needed to obtain representative simulations of diffusivity [45]. Experimental studies also showed that concrete samples with thickness of 10× the largest aggregate size is needed to obtain consistent permeability measurements due to drying-induced microcracking [46].

5 Conclusions

In the present work, the three-dimensional pore structure of a range of cementitious systems containing CEM I blended with silica fume, pulverised fuel ash or ground granulated blastfurnace slag cured to 7 and 90 days was imaged with an approach combining laser scanning confocal microscopy with serial sectioning and image reconstruction. The 3D pore structure (> 0.2 µm) was quantified to investigate the effects of axial distortion and to estimate the representative elementary volume (REV) of these systems. A total of 160 three-dimensional images were analysed. For each image, over twenty 3D pore parameters including total porosity, specific surface area, connectivity, skeleton tortuosity, diffusion tortuosity, formation factor, pore/throat radius, length, volume, shape factor and coordination number were quantified using BoneJ, maximal ball, cluster labelling and random walker algorithms. The main findings are summarised as follows:

a. The transition of brightness from the solid to the pore phases in LSCM images of cement-based materials spans across the entire grey scale due to the varying brightness of the solid phase. This complicates pore segmentation. The proposed pore segmentation method which combines the Moments method with CLAHE to enhance the local contrast of microstructures is able to segment pores as small as ≈ 0.2 µm with good accuracy.

b. Different cementitious systems tend to exhibit slightly different extents of axial distortion in LSCM images. Nevertheless, the axial distortion was found to have very minor effects on most of the measured pore parameters including total porosity, specific surface area, percolation connectivity, average pore and throat radii, and scalar diffusion tortuosity. A generic correction factor of 0.725 was proposed based on the measured aspect ratios of 80 PFA particles as a function of increasing axial compression.

c. Size of REV depends on the number of volumes sampled and averaged, the target % relative error and degree of variability (heterogeneity) of the pore structure. Based on the average results of four replicates, most pore parameters were found to be independent of the image volume size at 60^3 µm^3 except for diffusion tortuosity and formation factor. The REVs for porosity calculated based on eight realisations and a relative error of 5% for

different systems were all found to be ≤ 100^3 μm^3 except for P0.45 PFA 90d (101^3 μm^3), P0.45 SF 7d (107^3 μm^3) and P0.45 SF 90d (107^3 μm^3).

Acknowledgements

M.H.N. Yio would like to acknowledge the Dixon scholarship awarded by the Department of Civil and Environmental Engineering, Imperial College London. We thank Mr. Andrew Morris and Mr. Wenjie Zhou for their assistance with sample preparation and data collection.

References

[1] O. Rozenbaum, S.R. du Roscoat, Representative elementary volume assessment of three-dimensional x-ray microtomography images of heterogeneous materials: Application to limestones, Physical Review E, 89 (2014) 053304.

[2] J. Bear, Dynamics of fluids in porous media, American Elsevier Publishing Company, New York, 1972.

[3] E.J. Garboczi, D.P. Bentz, The effect of statistical fluctuation, finite size error, and digital resolution on the phase percolation and transport properties of the NIST cement hydration model, Cement and Concrete Research, 31 (2001) 1501-1514.

[4] M.Z. Zhang, G. Ye, K. van Breugel, A numerical-statistical approach to determining the representative elementary volume (REV) of cement paste for measuring diffusivity, 2010, 60 (2010) 14.

[5] N. Ukrainczyk, E.A.B. Koenders, Representative elementary volumes for 3D modeling of mass transport in cementitious materials, Modelling and Simulation in Materials Science and Engineering, 22 (2014) 035001.

[6] M.H.N. Yio, M.J. Mac, H.S. Wong, N.R. Buenfeld, 3D imaging of cement-based materials at submicron resolution by combining laser scanning confocal microscopy with serial sectioning, Journal of Microscopy, 258 (2015) 151-169.

[7] J.T. Fredrich, 3D imaging of porous media using laser scanning confocal microscopy with application to microscale transport processes, Physics and Chemistry of the Earth, Part A: Solid Earth and Geodesy, 24 (1999) 551-561.

[8] W. Oh, B. Lindquist, Image thresholding by indicator kriging, IEEE Transactions on Pattern Analysis and Machine Intelligence, 21 (1999) 590-602.

[9] W.M. Zhang, W. Sun, H.S. Chen, 3D visualisation of pore structures in cement-based materials by LSCM, Advances in Cement Research, 22 (2010) 53-57.

[10] J.B. Pawley, Handbook of biological confocal microscopy, Springer1995.

[11] L.A. Blatter, Cell volume measurements by fluorescence confocal microscopy: Theoretical and practical aspects, Methods in Enzymology, Academic Press1999, pp. 274-295.

[12] G.C. Sieck, C.B. Mantilla, Y.S. Prakash, Volume measurements in confocal microscopy, Methods in Enzymology, Academic Press1999, pp. 296-315.

[13] J.D. Gray, P. Kolesik, P.B. Høj, And, B.G. Coombe, Confocal measurement of the three-dimensional size and shape of plant parenchyma cells in a developing fruit tissue, The Plant Journal, 19 (1999) 229-236.

[14] British Standards Institution, BS EN 480-4:2005, Admixtures for concrete, mortar and grout. Test methods. Determination of bleeding of concrete, British Standards Institution, 2005.

[15] H.S. Wong, N.R. Buenfeld, Patch microstructure in cement-based materials: Fact or artefact?, Cement and Concrete Research, 36 (2006) 990-997.

[16] P. Thevenaz, U.E. Ruttimann, M. Unser, A pyramid approach to subpixel registration based on intensity, IEEE Transactions on Image Processing, 7 (1998) 27-41.

[17] S. Preibisch, S. Saalfeld, P. Tomancak, Globally optimal stitching of tiled 3D microscopic image acquisitions, Bioinformatics, 25 (2009) 1463-1465.

[18] H.S. Wong, M.K. Head, N.R. Buenfeld, Pore segmentation of cement-based materials from backscattered electron images, Cement and Concrete Research, 36 (2006) 1083-1090.

[19] M.H.N. Yio, H.S. Wong, N.R. Buenfeld, 3D Monte Carlo simulation of backscattered electron signal variation across pore-solid boundaries in cement-based materials, Cement and Concrete Research, 89 (2016) 320-331.

[20] N. Otsu, A threshold selection method from gray-level histograms, Automatica, 11 (1975) 23-27.

[21] T.W. Ridler, S. Calvard, Picture Thresholding Using an Iterative Selection Method, IEEE Transactions on Systems, Man, and Cybernetics, 8 (1978) 630-632.

[22] J.N. Kapur, P.K. Sahoo, A.K.C. Wong, A new method for gray-level picture thresholding using the entropy of the histogram, Computer Vision, Graphics, and Image Processing, 29 (1985) 273-285.

[23] G.W. Zack, W.E. Rogers, S.A. Latt, Automatic measurement of sister chromatid exchange frequency, Journal of Histochemistry & Cytochemistry, 25 (1977) 741-753.

[24] W.-H. Tsai, Moment-preserving thresolding: A new approach, Computer Vision, Graphics, and Image Processing, 29 (1985) 377-393.

[25] R. Mukundan, K. Ramakrishnan, Moment functions in image analysis: theory and applications, World Scientific1998.

[26] D. Hlushkou, S. Bruns, U. Tallarek, High-performance computing of flow and transport in physically reconstructed silica monoliths, Journal of Chromatography A, 1217 (2010) 3674-3682.

[27] K. Zuiderveld, Contrast limited adaptive histogram equalization, in: S.H. Paul (Ed.) Graphics gems IV, Academic Press Professional, Inc.1994, pp. 474-485.

[28] J. Schindelin, I. Arganda-Carreras, E. Frise, V. Kaynig, M. Longair, T. Pietzsch, S. Preibisch, C. Rueden, S. Saalfeld, B. Schmid, J.-Y. Tinevez, D.J. White, V. Hartenstein, K. Eliceiri, P. Tomancak, A. Cardona, Fiji: an open-source platform for biological-image analysis, Nat Meth, 9 (2012) 676-682.

[29] M. Doube, M.M. Kłosowski, I. Arganda-Carreras, F.P. Cordelières, R.P. Dougherty, J.S. Jackson, B. Schmid, J.R. Hutchinson, S.J. Shefelbine, BoneJ: Free and extensible bone image analysis in ImageJ, Bone, 47 (2010) 1076-1079.

[30] T.C. Lee, R.L. Kashyap, C.N. Chu, Building skeleton models via 3-D medial surface axis thinning algorithms, CVGIP: Graphical Models and Image Processing, 56 (1994) 462-478.

[31] H. Dong, M.J. Blunt, Pore-network extraction from micro-computerized-tomography images, Physical Review E, 80 (2009) 036307.

[32] Y. Nakashima, S. Kamiya, Mathematica programs for the analysis of three-dimensional pore connectivity and anisotropic tortuosity of porous rocks using X-ray computed tomography image data, Journal of Nuclear Science and Technology, 44 (2007) 1233-1247.

[33] L. Luo, H. Lin, S. Li, Quantification of 3-D soil macropore networks in different soil types and land uses using computed tomography, Journal of Hydrology, 393 (2010) 53-64.

[34] S.J. Pirson, Geologic well log analysis, Gulf Publishing, Houston, Texas, 1983.

[35] A. Atkinson, A.K. Nickerson, The diffusion of ions through water-saturated cement, Journal of Materials Science, 19 (1984) 3068-3078.

[36] E.J. Garboczi, Permeability, diffusivity, and microstructural parameters: A critical review, Cement and Concrete Research, 20 (1990) 591-601.

[37] A.A. Garrouch, L. Ali, F. Qasem, Using Diffusion and Electrical Measurements to Assess Tortuosity of Porous Media, Industrial & Engineering Chemistry Research, 40 (2001) 4363-4369.

[38] T. Kanit, S. Forest, I. Galliet, V. Mounoury, D. Jeulin, Determination of the size of the representative volume element for random composites: statistical and numerical approach, International Journal of Solids and Structures, 40 (2003) 3647-3679.

[39] S. Rolland du Roscoat, M. Decain, X. Thibault, C. Geindreau, J.F. Bloch, Estimation of microstructural properties from synchrotron X-ray microtomography and determination of the REV in paper materials, Acta Materialia, 55 (2007) 2841-2850.

[40] M.K. Head, H.S. Wong, N.R. Buenfeld, Characterisation of 'Hadley' grains by confocal microscopy, Cement and Concrete Research, 36 (2006) 1483-1489.

[41] J. Ollion, J. Cochennec, F. Loll, C. Escudé, T. Boudier, TANGO: a generic tool for high-throughput 3D image analysis for studying nuclear organization, Bioinformatics, (2013) btt276.

[42] A.C.A. Muller, K.L. Scrivener, A reassessment of mercury intrusion porosimetry by comparison with 1H NMR relaxometry, Cement and Concrete Research, 100 (2017) 350-360.

[43] A.C.A. Muller, K.L. Scrivener, A.M. Gajewicz, P.J. McDonald, Densification of C–S–H Measured by 1H NMR Relaxometry, The Journal of Physical Chemistry C, 117 (2013) 403-412.

[44] F. Mendoza, P. Verboven, H.K. Mebatsion, G. Kerckhofs, M. Wevers, B. Nicolaï, Three-dimensional pore space quantification of apple tissue using X-ray computed microtomography, Planta, 226 (2007) 559-570.

[45] S.D. Abyaneh, H.S. Wong, N.R. Buenfeld, Modelling the diffusivity of mortar and concrete using a three-dimensional mesostructure with several aggregate shapes, Computational Materials Science, 78 (2013) 63-73.

[46] Z. Wu, H.S. Wong, N.R. Buenfeld, Influence of drying-induced microcracking and related size effects on mass transport properties of concrete, Cement and Concrete Research, 68 (2015) 35-48.

Appendix I

The Moments method proposed by Tsai [24] considers the grey-level image as a blurred version of the binarised image. It computes the threshold of an image by retaining the first three moments of the original image in the binarised image. The first three moments of an image are calculated as:

$$m_i = \frac{1}{N}\sum_j N_j \left(z_j\right)^i = \sum_j p_j \left(z_j\right)^i \qquad \text{with } i = 1, 2, 3 \qquad \text{Eq. (I.1)}$$

Where N is the total number of pixels in the image, N_j is the total number of pixels with grey value z_j, and $p_j = N_j / N$. For bi-level thresholding, the pixels of the image are grouped into two classes, below- and above-threshold pixels. The moments of the binarised image m_i' are expressed as:

$$m_i^{'} = p_0 z_0^i + p_1 z_1^i \qquad \text{Eq. (I.2)}$$

Where p_0 and p_1 are the fractions and z_o and z_1 are the replacement grey values representative of the below- and above-threshold pixels respectively. By keeping the moments unchanged, $m_i = m_i^{'}$ and by solving Eq. (I.2) for m_i, p_0 and p_1, z_0^i and z_1^i can be determined. The threshold is taken as the grey value which corresponds to the p_0-tile of the histogram.

Appendix II

Table II.1: Effect of axial compression (at 0.25) on measured pore parameters for all samples. Results are normalised to that of no compression.

Sample ID	Age (days)	BoneJ							Maximal ball							
		Total porosity	Accessible porosity	Percolation connectivity	Euler connectivity	Mesh specific surface area	Skeleton tortuosity	Avg. pore size	Avg. pore shape factor	Avg. pore connection number	Avg. pore volume	Avg. pore radius	Avg. throat shape factor	Avg. throat length	Avg. throat radius	Avg. throat volume
P0.45	7	1.00	1.00	1.00	2.05	1.26	1.00	0.79	0.91	1.00	0.50	1.02	1.00	0.78	0.96	0.46
	90	0.99	0.99	1.00	2.45	1.33	1.01	0.75	0.96	0.97	0.40	0.86	1.00	0.74	0.81	0.39
P0.45 SF	7	0.99	0.99	1.00	2.19	1.26	1.01	0.80	0.93	0.96	0.48	0.92	1.00	0.74	0.86	0.48
	90	0.99	0.98	0.99	2.22	1.25	1.02	0.83	0.91	0.87	0.41	0.91	1.00	0.67	0.85	0.43
P0.45 PFA	7	1.00	1.00	1.00	2.86	1.43	1.01	0.65	0.95	1.10	0.41	0.87	1.00	0.83	0.81	0.41
	90	0.99	0.99	1.00	2.07	1.30	1.01	0.77	0.93	0.91	0.44	0.94	1.01	0.76	0.91	0.44
P0.45 GGBS	7	1.00	0.99	1.00	1.91	1.29	1.01	0.74	0.92	0.98	0.48	1.02	1.00	0.81	0.96	0.50
	90	0.99	0.99	0.99	2.09	1.28	1.01	0.78	0.95	0.92	0.42	0.90	1.00	0.75	0.85	0.41
Average		0.99	0.99	1.00	2.23	1.30	1.01	0.76	0.93	0.97	0.44	0.93	1.00	0.76	0.88	0.44

Sample ID	Age (days)	Cluster labelling and random walker						
		Voxel S_p A	Voxel S_p B	Diffusion tortuosity X	Diffusion tortuosity Y	Diffusion tortuosity Z	Scalar diffusion tortuosity	Formation factor
P0.45	7	1.28	1.29	0.52	0.49	2.97	1.12	1.13
	90	1.35	1.36	0.54	0.66	3.94	1.13	1.14
P0.45 SF	7	1.29	1.30	0.56	0.57	3.24	1.23	1.24
	90	1.29	1.30	0.58	0.49	3.66	1.54	1.56
P0.45 PFA	7	1.44	1.44	0.60	0.58	3.24	1.12	1.13
	90	1.33	1.33	0.75	0.48	10.97	1.10	1.11
P0.45 GGBS	7	1.31	1.32	0.48	0.47	3.25	1.18	1.19
	90	1.31	1.32	0.58	0.65	3.92	1.67	1.70
Average		1.32	1.33	0.58	0.55	4.40	1.26	1.27

Cement & Concrete Research (2017) Accepted
https://doi.org/10.1016/j.cemconres.2017.09.012

Representative elementary volume (REV) of cementitious materials from three-dimensional pore structure analysis

M.H.N. Yio, H.S. Wong* and N.R. Buenfeld

Concrete Durability Group, Department of Civil and Environmental Engineering, Imperial College London, SW7 2AZ, UK

Table 1: Mix proportions.

Sample ID	CEM I (kg/m^3)	SCM (wt.% total binder)	SF (kg/m^3)	PFA (kg/m^3)	GGBS (kg/m^3)	Water (kg/m^3)	Total w/b	Free w/b*
P0.45	1290	-	-	-	-	581	0.45	0.426
P0.45 SF	1158	9	115	-	-	573	0.45	0.445
P0.45 PFA	965	23	-	288	-	564	0.45	0.434
P0.45 GGBS	505	60	-	-	758	568	0.45	0.415

** After correcting for water lost to bleeding*

Table 2: Oxide compositions and properties of cementitious materials used.

Binder	Oxide composition (wt.%)									LOI (%)	Laser granulometry d_{50} (μm)
	CaO	SiO_2	Al_2O_3	Fe_2O_3	MgO	$Na_2O_{(eq)}$	K_2O	SO_3	Cl^-		
CEM I	63.4	20.8	5.4	2.4	1.5	0.3	0.7	2.9	<0.1	2.10	N/A
SF	0.2	98.6	0.3	0.0	0.1	0.2	-	0.1	-	N/A	0.25
PFA	0.1	72.2	24.3	0.4	0.1	0.3	-	0.1	-	N/A	7.00
GGBS	40.8	36.5	11.6	1.4	7.5	0.5	-	2.1	-	-0.99	8.00

Table 3: Details of the 3D pore reconstruction.

Sample ID	XY field of view (μm^2)		Total number of stacks		Total reconstructed thickness (μm)		Average overlapping region (%)		Average R	
	A	B	A	B	A	B	A	B	A	B
P0.45 7d	190 × 190	161 × 186	52	62	117	137	42.0	42.1	0.93	0.93
P0.45 90d	190 × 190	190 × 190	44	40	143	130	37.4	38.4	0.92	0.93
P0.45 SF 7d	190 × 190	190 × 136	43	40	142	141	35.1	35.6	0.88	0.88
P0.45 SF 90d	190 × 190	188 × 188	47	47	144	148	39.0	39.4	0.90	0.90
P0.45 PFA 7d	190 × 190	190 × 190	62	56	146	138	43.1	42.9	0.89	0.89
P0.45 PFA 90d	190 × 190	190 × 190	43	42	147	150	34.3	36.2	0.89	0.90
P0.45 GGBS 7d	190 × 190	187 × 187	59	58	108	140	47.9	39.3	0.92	0.92
P0.45 GGBS 90d	190 × 129	180 × 180	43	44	141	145	37.8	37.9	0.88	0.87

* Corresponding author. Tel: +44 (0)20 7594 5956.

E-mail: hong.wong@imperial.ac.uk

Table 4: Quantification of 3D pore parameters using different methods.

Method	Software	Algorithm	Parameters
BoneJ (Doube et al., 2010)	Fiji (v.1.51d)	Voxel counting	Total segmented porosity (Φ) = total volume of pore / total volume of image × 100%
		Mapped labelling	• Accessible porosity (Φ_p) = volume of largest percolated pore in X, Y and Z / total volume of image × 100% • Percolation connectivity (X) = accessible porosity / total porosity
		Euler characteristic	Euler connectivity = 1 – $\Delta\chi$, where $\Delta\chi$ represents the contribution from largest connected pore (Odgaard and Gundersen, 1993)
		Marching cube	Mesh specific surface area (S_p) = surface area of pore mesh / volume of largest connected pore (m^{-1})
		3D medial surface axis thinning	Skeleton tortuosity of largest connected pore (τ_s) (see Eq. (1) in text)
		Thickness computing	Volume-weighted average pore size (thickness) of largest connected pore (m)
Modified maximal ball (Dong and Blunt, 2009)	Windows Command Prompt	Modified maximal ball	• Total segmented porosity (Φ) as in BoneJ; • Pore and throat radii: inscribed radii of the largest spheres in pores and throats respectively (m); • Throat length: see Figure 5 in Dong and Blunt (2009) (m); • Pore connection (coordination) number: number of pores linked to each pore defined; • Pore and throat volume: number of voxels associated with each pore or throat block defined (m^3); • Pore and throat shape factor = volume*length / surface area^2 of each pore or throat block defined
Mathematica programmes (Nakashima and Kamiya, 2007)	Mathematica® (v.10.4) (Wolfram Research, Champaign, Illinois)	Cluster labelling	• Total segmented porosity (Φ), accessible porosity (Φ_p) and percolation connectivity (X) as in BoneJ; • Voxel specific surface area (S_p) = surface area of voxels of largest connected pore without (A) and with (B) considering pore faces on the edges / volume of largest connected pore (m^{-1})
		Random walker	• Scalar (τ_D) and directional (τ_d) diffusion tortuosity of largest connected pore (see Eq. (2) in text); • Formation factor (F) of largest connected pore = τ_D^2 / Φ_p

Table 5: Details of 3D pore models used for validation.

Pore configurations	Model	Number of pore	Number of throat	Pore radius (voxel)	Pore centre to pore centre length (voxel)	Throat radius (voxel)
Pore attached	a	3	3	32	66	8
	b	4	6			
	c	8	12			
Pore linked by short throats	d	3	3	24	84	
	e	4	6			
	f	8	12			
Pore linked by long throats	g	3	3	16	104	
	h	4	6			
	i	8	12			

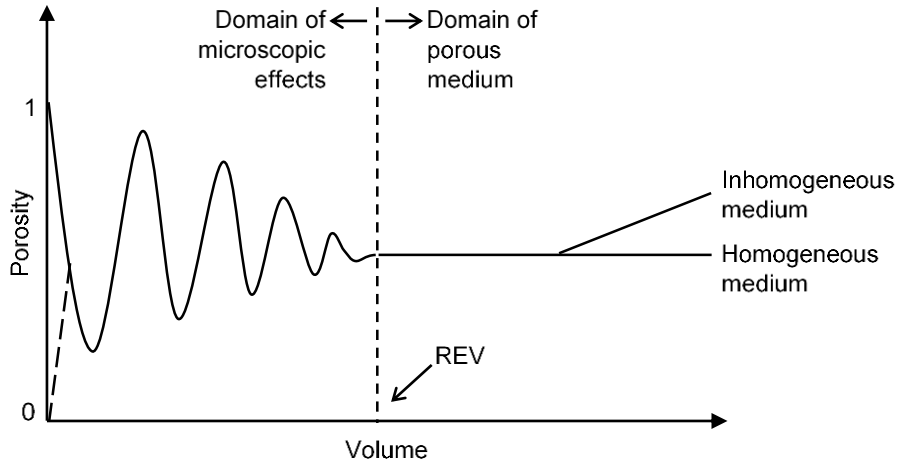

Figure 1: Change in property of interest (e.g. porosity) as a function of sample volume to define REV (after Bear [2]).

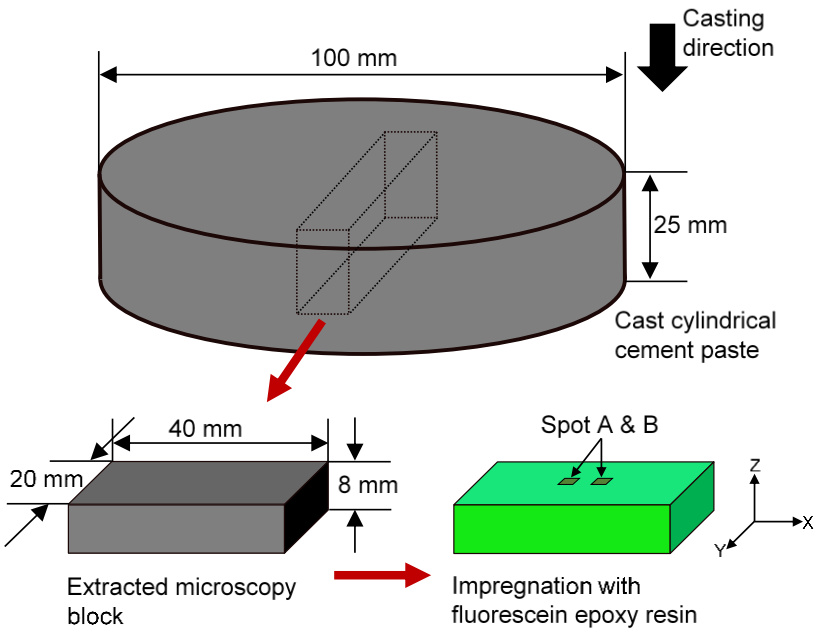

Figure 2: Preparation of epoxy impregnated block for 3D LSCM from cast cylindrical sample (not to scale).

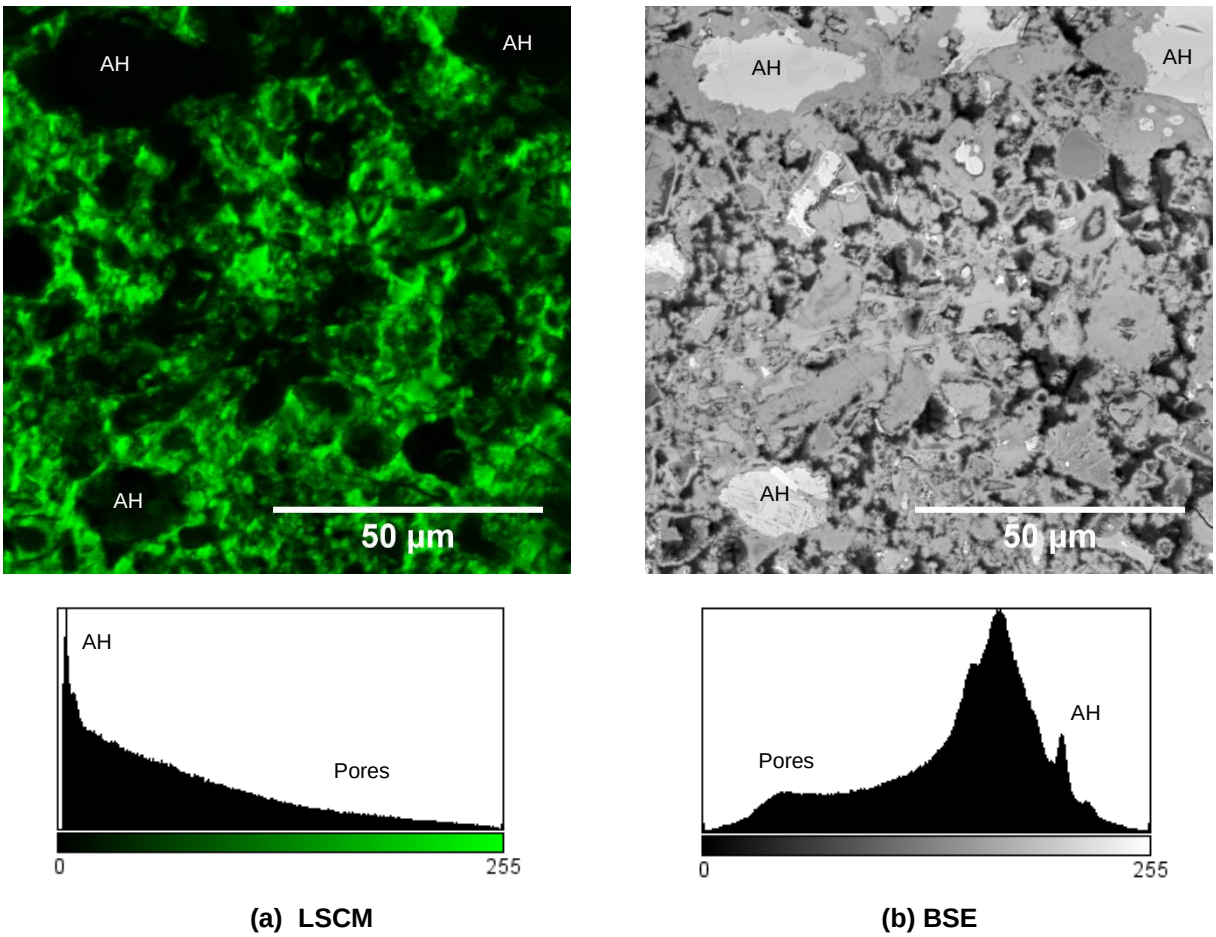

Figure 3: Comparison between LSCM and BSE images of hardened cement paste impregnated with fluorescein-doped epoxy captured at the same area. Sample is P0.45 7d.

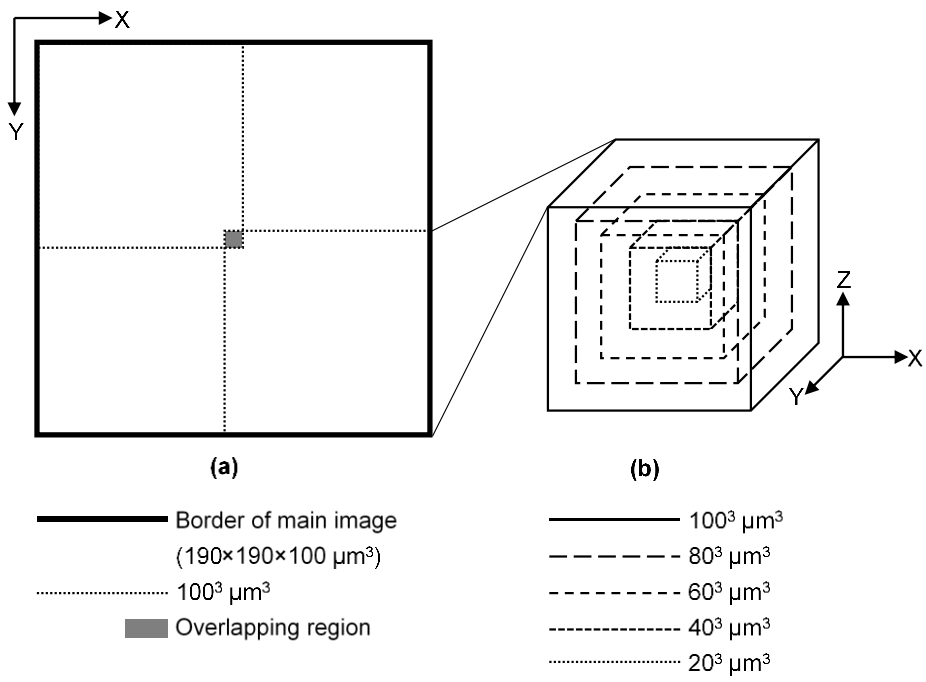

Figure 4: Cropping of sampling volumes from the main 3D image for REV analysis: (a) XY plane of the main 3D image; and (b) 3D views of cropped sampling volumes. Diagram not to scale.

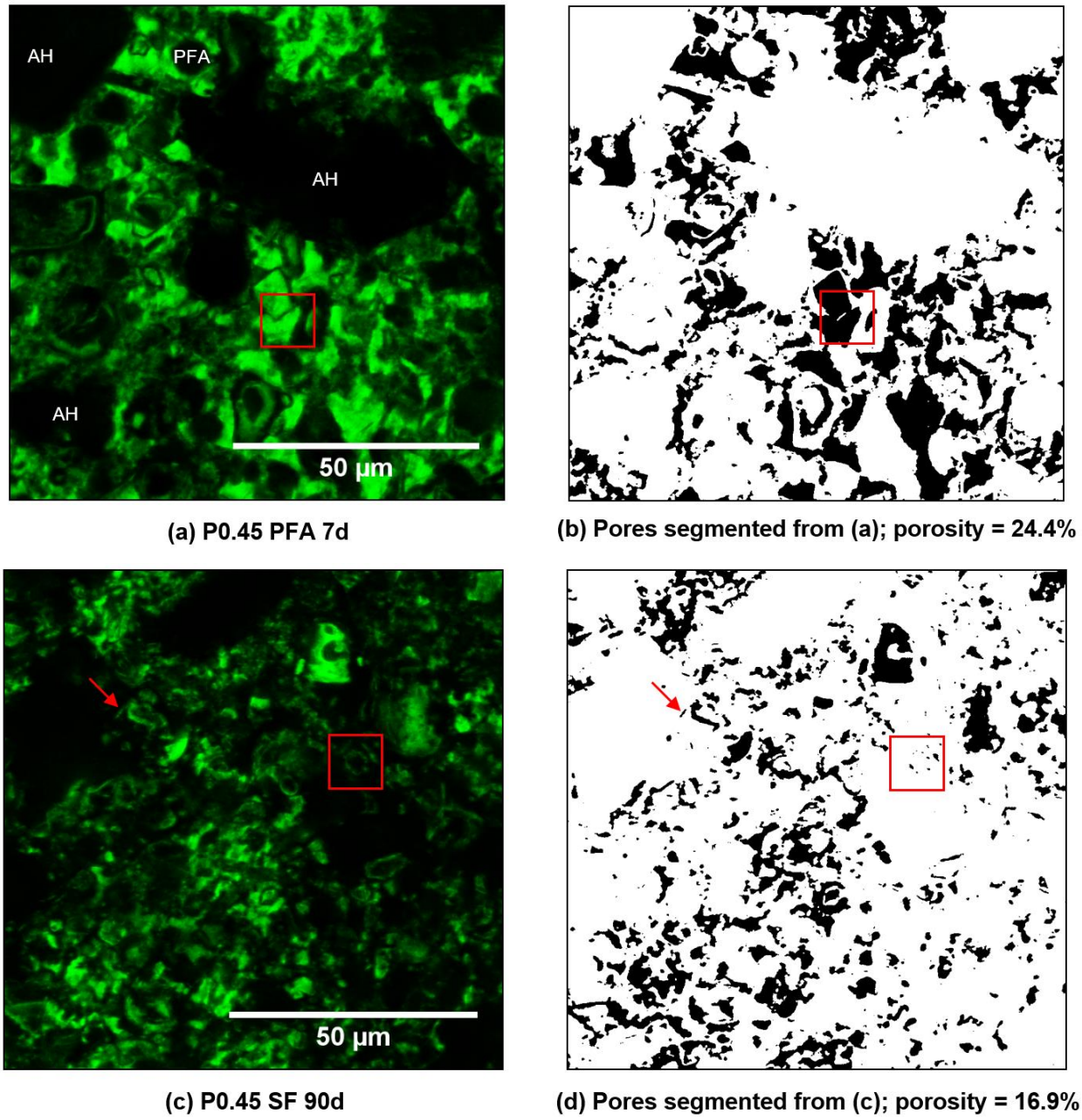

Figure 5: Example pore segmentation demonstrated on (a, b) P0.45 PFA 7d; and (c, d) P0.45 SF 90d.

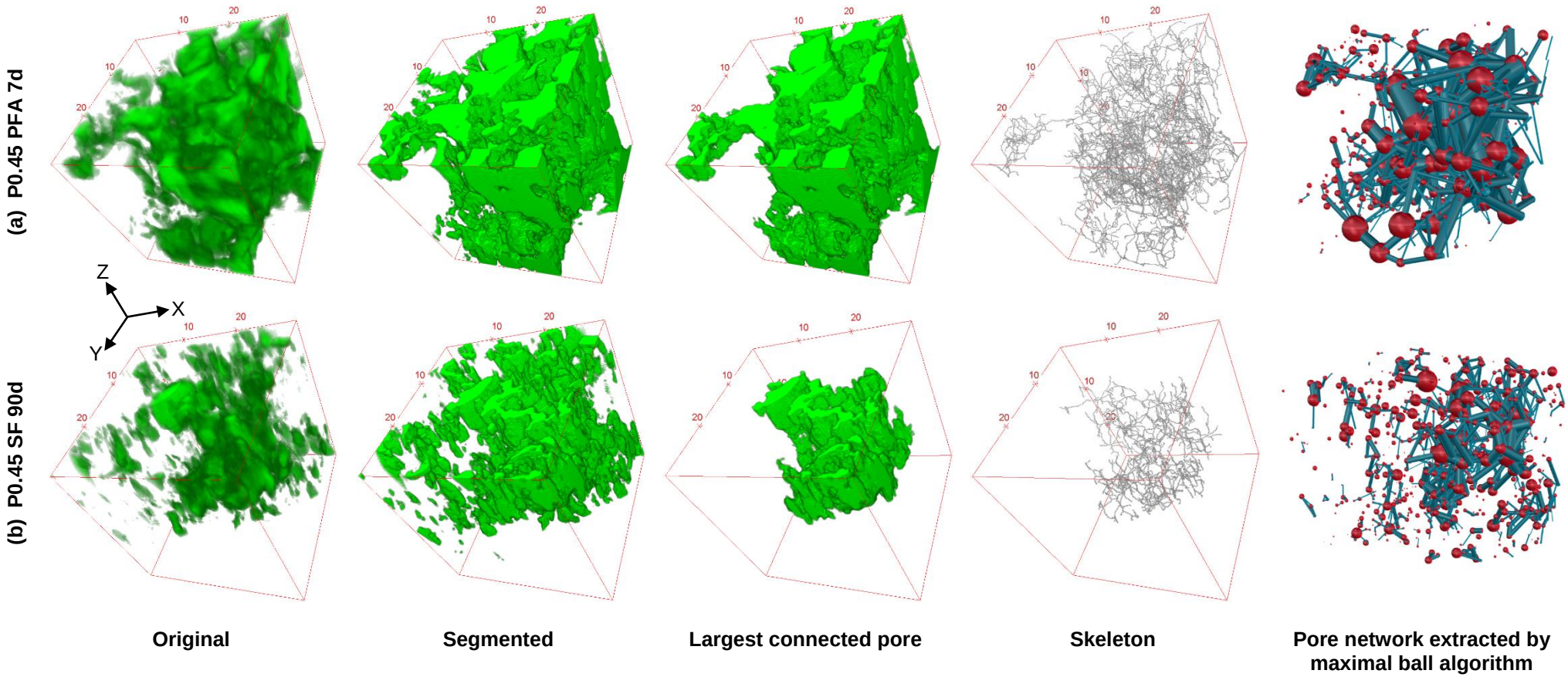

Figure 6: Example 3D views of the pore structure of (a) P0.45 PFA 7d; and (b) P0.45 SF 90d. All image volumes are 30^3 µm^3. Images were generated using Fiji except for the pore networks, which were visualised using Rhinoceros 5 (Robert McNeel & Associates, Seattle). In the pore networks, green cylinders represent pore throats while red spheres represent 'ancestor' pores.

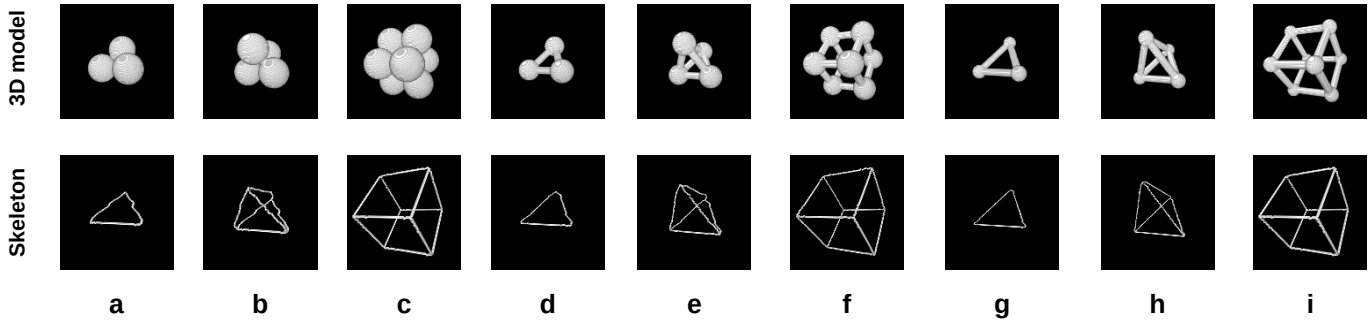

Figure 7: 3D pore models and their respective skeletons computed by the medial-axis thinning algorithm for validation.

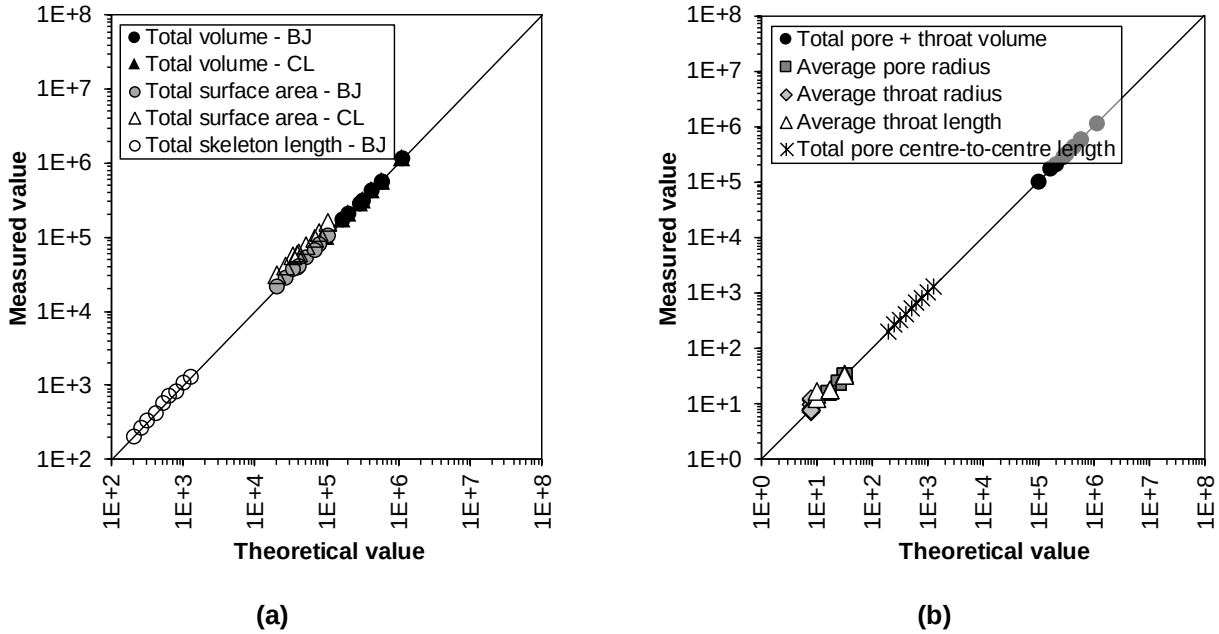

Figure 8: Comparison between measured pore parameters and theoretical values for the 3D pore models shown in Fig. 7. Measurements were made using (a) BoneJ (BJ) and cluster labelling (CL); (b) maximal ball algorithms.

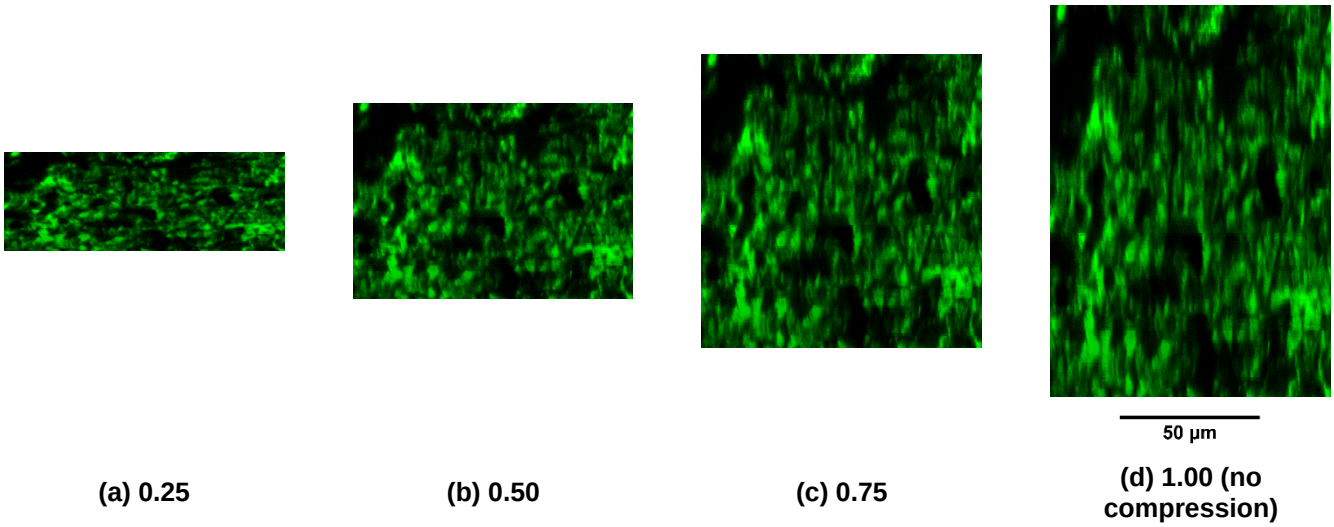

Figure 9: Applying axial compression to correct optical distortion in the Z axis of LSCM images. Sample is P0.45 7d.

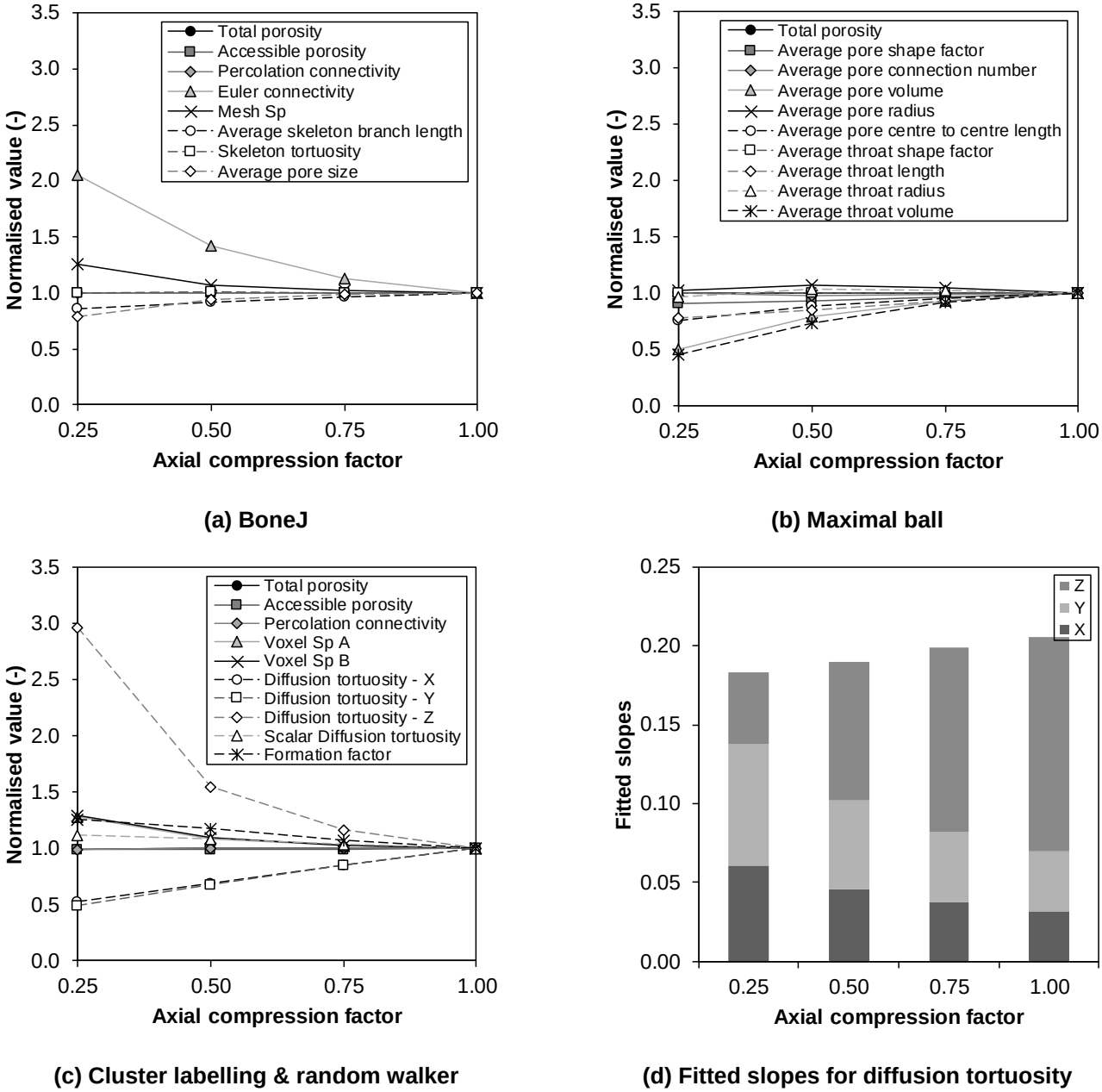

Figure 10: Effect of axial compression on pore parameters quantified with (a) BoneJ; (b) maximal ball; and (c) cluster labelling and random walker algorithms. Sample is P0.45 7d. (d) Contributions from X, Y and Z directions to the scalar diffusion tortuosity.

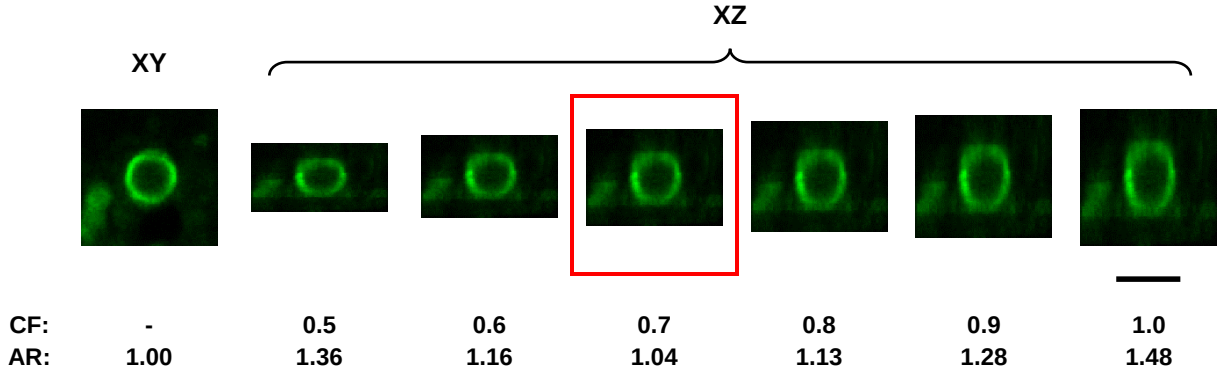

Figure 11: Determining the optimal compression factor (CF) for correcting axial distortion in the Z axis based on aspect ratio (AR) of spherical PFA particles. The compression factor giving the lowest aspect ratio is ~ 0.7. Scale bar is 5 µm. Sample is P0.45 PFA 90d.

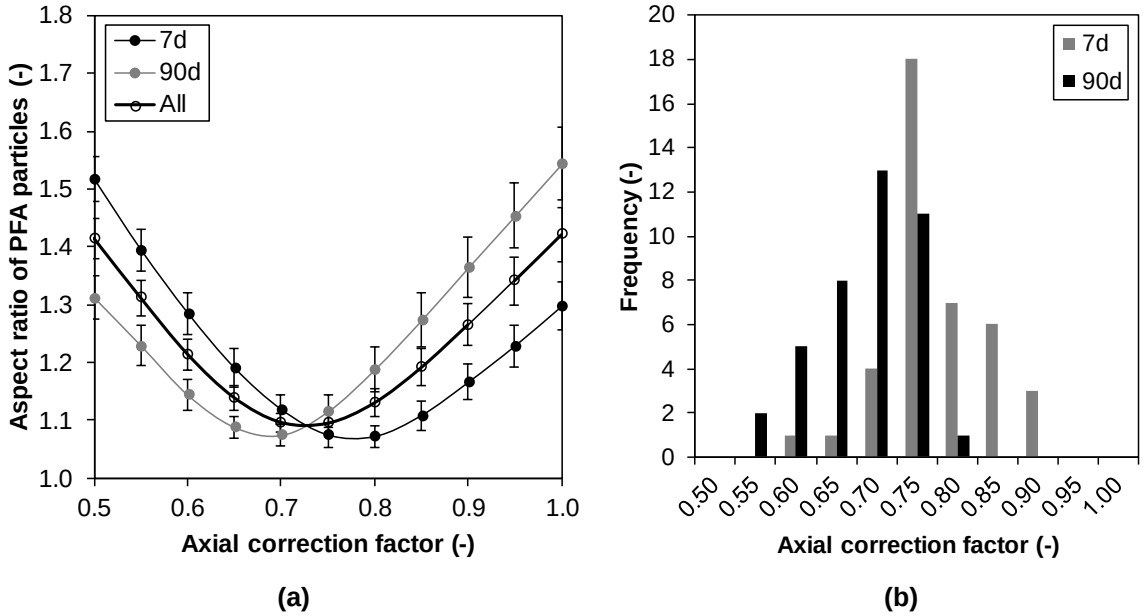

Figure 12: Results of 80 PFA particles from P0.45 PFA 7d and 90d: (a) average aspect ratio vs. axial compression factor; and (b) frequency histogram of axial compression factors giving the minimum aspect ratio of each PFA particle.

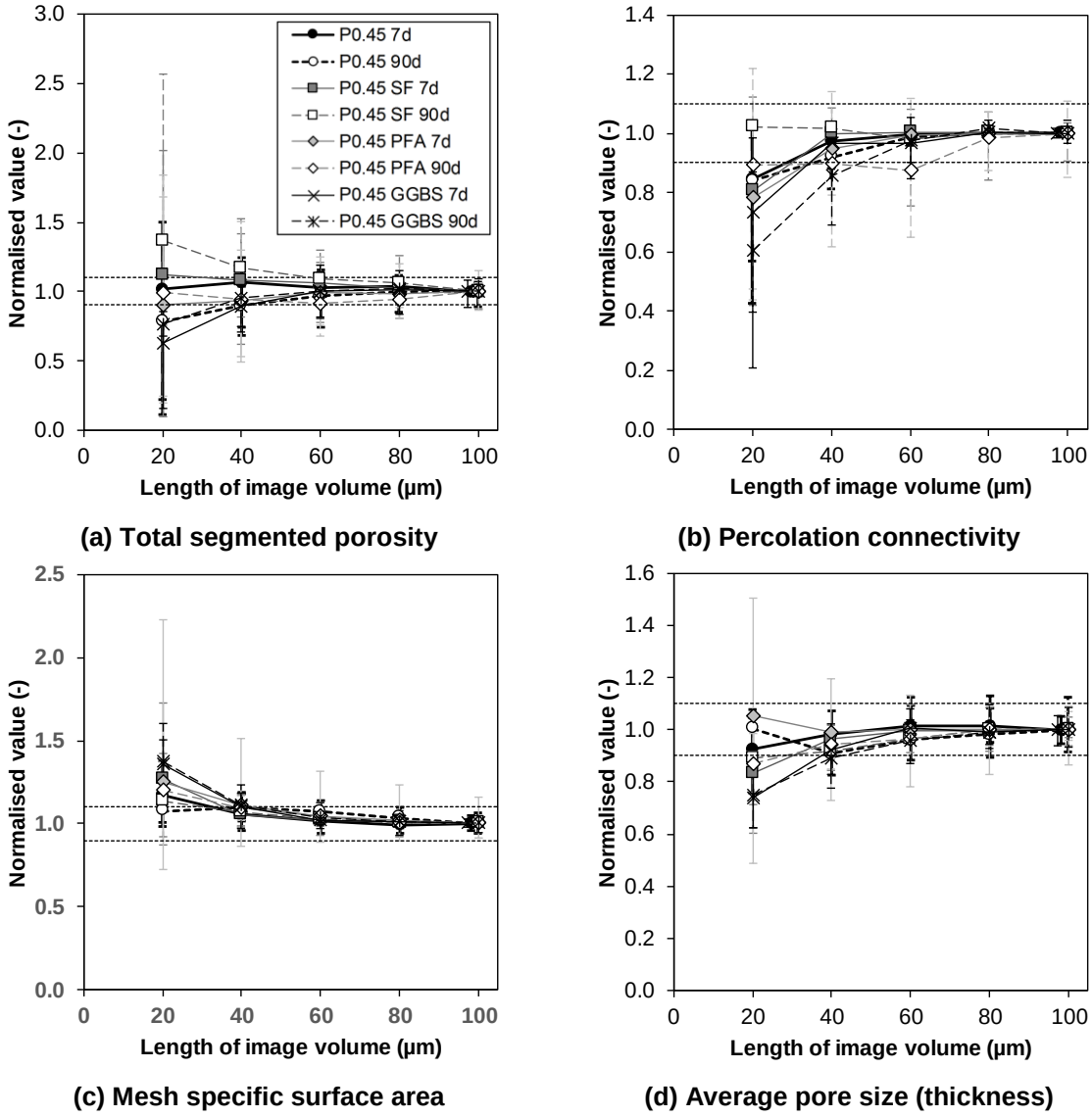

Figure 13: Change in (a) total porosity; (b) percolation connectivity; (c) mesh specific surface area; and (d) average pore size as a function of image volume size for all samples. Each data point is an average of four measurements and normalised to the value at 100^3 μm^3. Error bars show max/min values. Horizontal dashed lines mark the 0.9 to 1.0 boundaries.

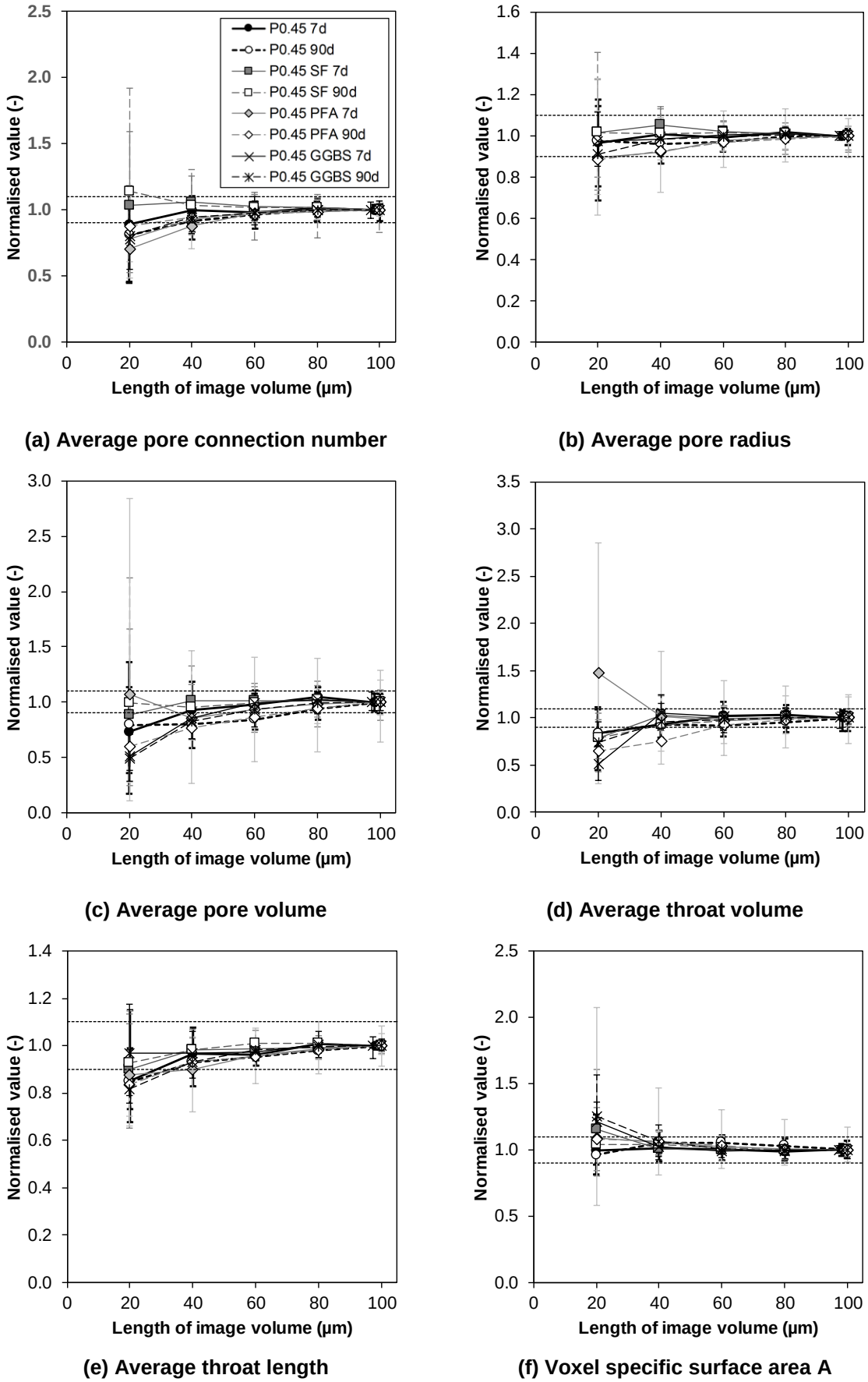

Figure 14: Change in (a) average pore connection number; (b) average pore radius; (c) average pore volume; (d) average throat volume; (e) average throat radius; and (f) voxel specific surface area as a function of image volume size for all samples. Each data point is an average of four measurements and normalised to that at 100^3 μm^3. Error bars show max/min values. Horizontal dashed lines mark the 0.9 to 1.0 boundaries.

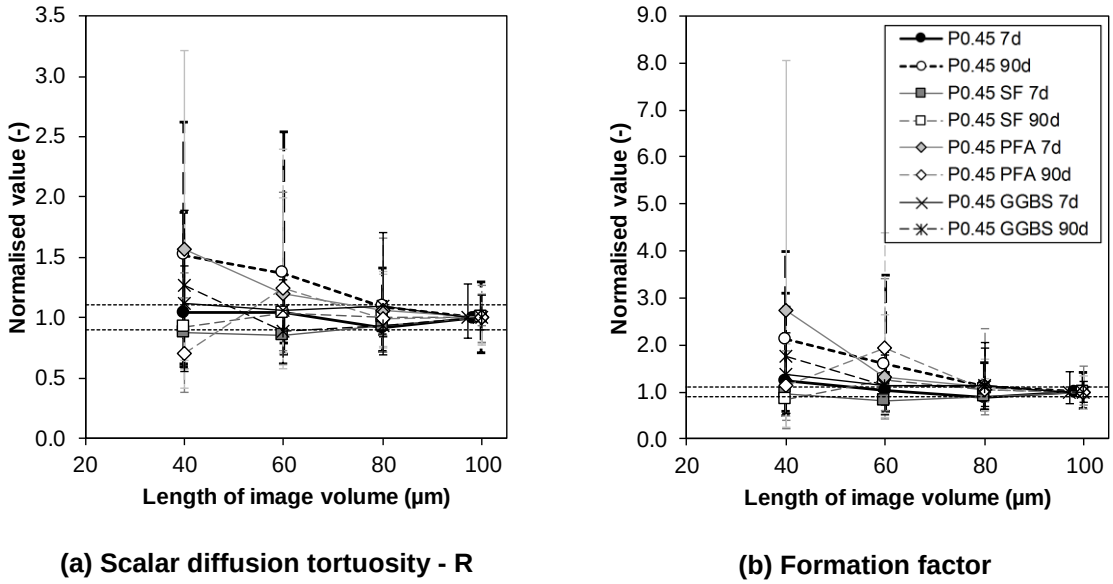

Figure 15: Change in (a) scalar diffusion tortuosity; and (b) formation factor as a function of image volume size for all samples. Each data point is an average of four measurements and normalised to that at 100^3 μm^3. Error bars show max/ min values. Horizontal dashed lines mark the 0.9 to 1.0 boundaries.

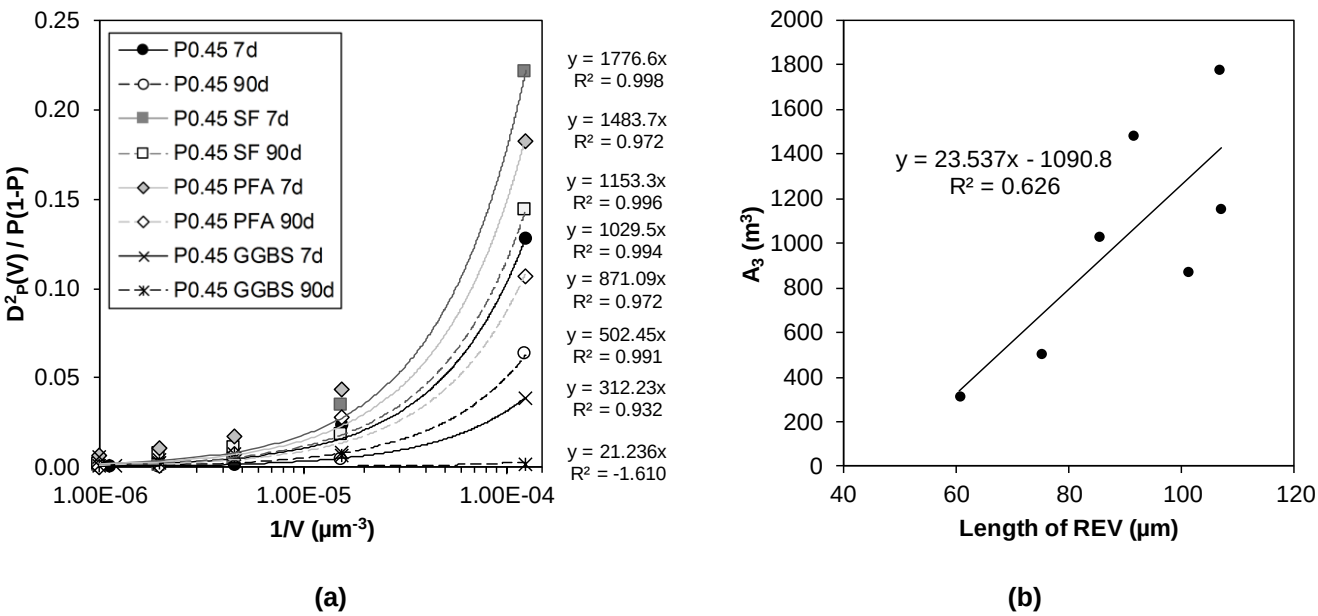

Figure 16: a) Determination of A_3 by curve fitting Eq. (5) to the variances of measured porosities as a function of image volume. Note that Eq. (5) has been rearranged so that the fitted slope gives A_3. b) Relation between A_3 and length of REV (n = 8; ε = 5%).

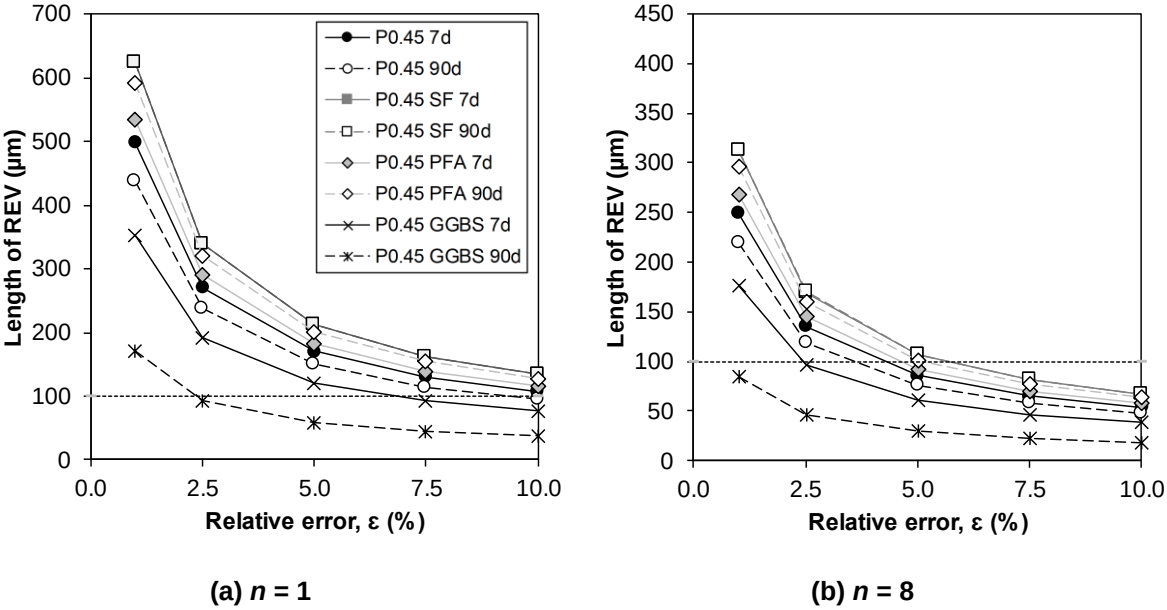

Figure 17: REV for porosity (Eq. 4) as a function of relative error ε for (a) $n = 1$, and (b) $n = 8$, where n is the number of realisations (number of image volumes analysed). Horizontal dashed lines mark the REV of 100^3 µm^3.

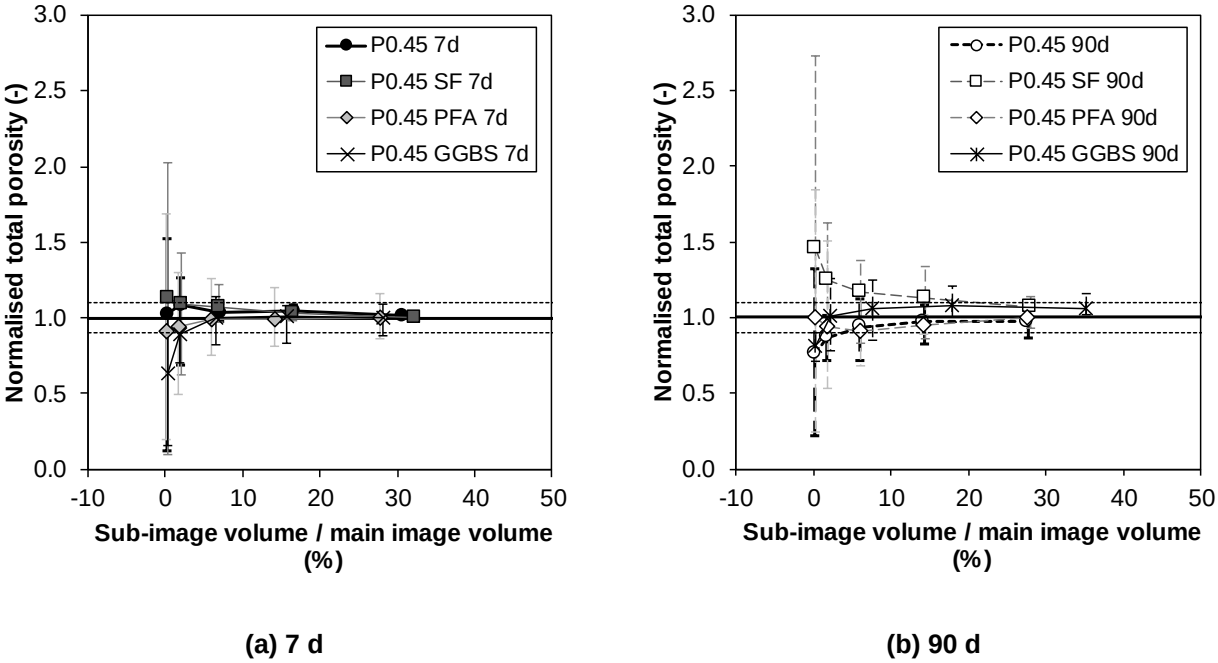

Figure 18: Total porosity measured from sampling volumes (20^3, 40^3, 60^3, 80^3 and 100^3 µm^3) normalised to that measured from the main image volumes (≈190×190×100 µm^3) plotted against ratio of sampling volume to the main image volume. Each data point is an average of four measurements. Error bars show the maximum and minimum values. Horizontal dashed lines mark the range from 0.9 to 1.0.